A. Abbà, L. Bonaventura, M. Nini, M. Restelli
Dynamic Models for Large Eddy Simulation of Compressible Flows with a High Order DG Method
Computers & Fluids, Vol. 122, 2015, p. 209-222
doi:10.1016/j.compfluid.2015.08.021

Dynamic models for Large Eddy Simulation of compressible flows with a high order DG method

A. Abbà[a], L. Bonaventura[b,*], M. Nini[a], M. Restelli[c]

[a] *Dipartimento di Scienze e Tecnologie Aerospaziali, Politecnico di Milano, Via La Masa 34, 20156 Milano, Italy*
[b] *MOX – Modelling and Scientific Computing, Dipartimento di Matematica, Politecnico di Milano, Via Bonardi 9, 20133 Milano, Italy*
[c] *NMPP – Numerische Methoden in der Plasmaphysik, Max–Planck–Institut für Plasmaphysik, Boltzmannstraße 2, D-85748 Garching, Germany*

Abstract

The impact of dynamic models for applications to LES of compressible flows is assessed in the framework of a numerical model based on high order discontinuous finite elements. The projections onto lower dimensional subspaces associated to lower degree basis function are used as LES filter, along the lines proposed in Variational Multiscale templates. Comparisons with DNS results available in the literature for plane and constricted channel flows at Mach numbers 0.2, 0.7 and 1.5 show clearly that the anisotropic model is able to reproduce well most key features of the flow.

Keywords: Turbulence modeling, Large Eddy Simulation, Discontinuous Galerkin methods, compressible flows, dynamic models

AMS Subject Classification: 65M60, 65Z05, 76F25, 76F50, 76F65

High order finite element methods are an extremely appealing framework to implement LES models of turbulent flows, due to their potential for reducing the impact of numerical dissipation on most of the spatial scales of interest. Discontinuous Galerkin (DG) methods have been applied to LES and DNS by several authors, see e.g. [10], [11], [13], [36], [51], [55], [56], [58]. DG methods are particularly appealing for realistic CFD applications for a number of practical and conceptual reasons. At a more practical level, they allow to implement h and p refinement procedures with great ease and to work on complex and also non conforming meshes. Even though they imply quite stringent stability restrictions for explicit time discretizations, a number of techniques is available to improve computational efficiency if required, see e.g. [18], [24], [45], [49], [54]. At a more conceptual level, discontinuous finite elements provide a natural framework to generalize LES filters to arbitrary computational meshes. As proposed in some of the previously quoted papers, the filter operator that is the key tool in LES can be identified with the projection operator on a finite dimensional space related to the discretization. This allows to generalize easily the LES concept to unstructured meshes and complex geometries. Ideas of this kind have first arisen in the framework of the Variational Multiscale (VMS) approach, which was introduced in [26] and applied to Large Eddy Simulation (LES) of incompressible flows in [27], [28], [29] (see also the review in [30]). Other multiscale approaches to LES in the framework of finite element discretizations have been

*Corresponding author
Email addresses: antonella.abba@polimi.it (A. Abbà), luca.bonaventura@polimi.it (L. Bonaventura), michele.nini@polimi.it (M. Nini), marco.restelli@ipp.mpg.de (M. Restelli)

proposed e.g. in [31], [32], [34], [44].

This very promising framework, however, seems to have been only partially exploited so far. In [56], for example, the LES filter has been realized by face based projection operators that are different from those for which the VMS template has been outlined in [13]. Furthermore, to the best of our knowledge, only simple Smagorinsky closures have been employed to model the subgrid stresses in the previously cited VMS approaches. In this paper, we investigate the potential benefit resulting from the use of dynamic subgrid scale models in a VMS-DG framework. We consider both standard isotropic models and the anisotropic dynamic model [2], appropriately extended to the compressible case. Anisotropic models try to address the failure of the Boussinesq hypothesis (see e.g. [48] for an extensive review of this subject) by introducing a tensor valued subgrid viscosity, thus avoiding alignment of the stress and velocity strain rate tensors. We implement a LES model with projection-based filter in the framework of a high order DG method and we assess the performance of this more sophisticated subgrid closure with respect to the simple Smagorinsky closure and to more standard isotropic dynamic models. The comparison is carried out with respect to the DNS experiment results reported in [6], [9], [43] and [58]. Both isotropic and anisotropic dynamic models show a clear improvement in the prediction of several key features of the flow with respect to the Smagorinsky closure implemented in the same framework. In particular, the dynamic models allow to achieve a better representation of mean quantities profiles, turbulent stresses and, more generally, of the total turbulent kinetic energy.

In section 1, the Navier-Stokes equations for compressible flow are recalled. In section 3, the DG finite element discretization is reviewed. In section 2, the LES models employed are described, while in section 4 the results of our comparisons with DNS data are reported. Some conclusions and perspectives for future work are presented in section 5.

1. Model equations

We consider the compressible Navier–Stokes equations, which, employing the Einstein notation, can be written in dimensional form (denoted by the superscript "d") as

$$\partial_{t^{\mathrm{d}}}\rho^{\mathrm{d}} + \partial_{x_j^{\mathrm{d}}}(\rho^{\mathrm{d}} u_j^{\mathrm{d}}) = 0 \tag{1a}$$

$$\partial_{t^{\mathrm{d}}}(\rho^{\mathrm{d}} u_i^{\mathrm{d}}) + \partial_{x_j^{\mathrm{d}}}(\rho^{\mathrm{d}} u_i^{\mathrm{d}} u_j^{\mathrm{d}}) + \partial_{x_i^{\mathrm{d}}} p^{\mathrm{d}} - \partial_{x_j^{\mathrm{d}}}\sigma_{ij}^{\mathrm{d}} = \rho^{\mathrm{d}} f_i^{\mathrm{d}} \tag{1b}$$

$$\partial_{t^{\mathrm{d}}}(\rho^{\mathrm{d}} e^{\mathrm{d}}) + \partial_{x_j^{\mathrm{d}}}(\rho^{\mathrm{d}} h^{\mathrm{d}} u_j^{\mathrm{d}}) - \partial_{x_j^{\mathrm{d}}}(u_i^{\mathrm{d}}\sigma_{ij}^{\mathrm{d}}) + \partial_{x_j^{\mathrm{d}}} q_j^{\mathrm{d}} = \rho^{\mathrm{d}} f_j^{\mathrm{d}} u_j^{\mathrm{d}}, \tag{1c}$$

where ρ^{d}, $\mathbf{u}^{\mathrm{d}}$ and e^{d} denote density, velocity and specific total energy, respectively, p^{d} is the pressure, $\mathbf{f}^{\mathrm{d}}$ is a prescribed forcing, h^{d} is the specific enthalpy, defined by $\rho^{\mathrm{d}} h^{\mathrm{d}} = \rho^{\mathrm{d}} e^{\mathrm{d}} + p^{\mathrm{d}}$, and σ^{d} and $\mathbf{q}^{\mathrm{d}}$ are the diffusive momentum and heat fluxes. Equation (1) must be complemented with the state equation

$$p^{\mathrm{d}} = \rho^{\mathrm{d}} R T^{\mathrm{d}}, \tag{2}$$

where T^{d} is the temperature and R is the ideal gas constant. The temperature can then be expressed in terms of the prognostic variables introducing the specific internal energy $e_{\mathrm{i}}^{\mathrm{d}}$, so that

$$e^{\mathrm{d}} = e_{\mathrm{i}}^{\mathrm{d}} + \frac{1}{2} u_k^{\mathrm{d}} u_k^{\mathrm{d}}, \qquad e_{\mathrm{i}}^{\mathrm{d}} = c_v T^{\mathrm{d}}, \tag{3}$$

where c_v is the specific heat at constant volume. Finally, the model is closed with the constitutive equations for the diffusive fluxes:

$$\sigma_{ij}^{\mathrm{d}} = \mu^{\mathrm{d}} \mathcal{S}_{ij}^{d,\mathrm{d}}, \qquad q_i^{\mathrm{d}} = -\frac{\mu^{\mathrm{d}} c_p}{Pr} \partial_{x_i^{\mathrm{d}}} T^{\mathrm{d}}, \tag{4}$$

where $\mathcal{S}_{ij}^{\mathrm{d}} = \partial_{x_j^{\mathrm{d}}} u_i^{\mathrm{d}} + \partial_{x_i^{\mathrm{d}}} u_j^{\mathrm{d}}$ and $\mathcal{S}_{ij}^{d,\mathrm{d}} = \mathcal{S}_{ij}^{\mathrm{d}} - \frac{1}{3}\mathcal{S}_{kk}^{\mathrm{d}}\delta_{ij}$, the specific heat at constant pressure is $c_p = R + c_v$, Pr denotes the Prandtl number, and the dynamic viscosity μ^d is assumed to depend only on temperature T^d according to the power law

$$\mu^{\mathrm{d}}(T^{\mathrm{d}}) = \mu_0^{\mathrm{d}} \left(\frac{T^{\mathrm{d}}}{T_0^{\mathrm{d}}} \right)^{\alpha}, \tag{5}$$

in agreement with Sutherland's hypothesis (see e.g. [47]) with $\alpha = 0.7$. The dimensionless form of the problem is obtained assuming reference quantities ρ_r, L_r, V_r and T_r, as well as

$$\begin{aligned} &t_r = \tfrac{L_r}{V_r}, \quad p_r = \rho_r R T_r, \quad \sigma_r = \tfrac{\mu_r V_r}{L_r}, \quad f_r = \tfrac{V_r^2}{L_r}, \\ &e_r = R T_r, \quad q_r = \tfrac{\mu_r c_p T_r}{Pr\, L_r}, \quad \mu_r = \mu_0^{\mathrm{d}} \left(\tfrac{T_r}{T_0^{\mathrm{d}}} \right)^{\alpha}. \end{aligned} \tag{6}$$

Defining now

$$\begin{aligned} &\rho^{\mathrm{d}} = \rho_r \rho, \quad u_i^{\mathrm{d}} = V_r u_i, \quad T^{\mathrm{d}} = T_r T, \\ &t_r \partial_{t^{\mathrm{d}}} = \partial_t, \quad L_r \partial_{x_i^{\mathrm{d}}} = \partial_i, \\ &p^{\mathrm{d}} = p_r p, \quad \sigma_{ij}^{\mathrm{d}} = \sigma_r \sigma_{ij}, \quad f^{\mathrm{d}} = f_r f, \\ &e^{\mathrm{d}} = e_r e, \quad q^{\mathrm{d}} = q_r q, \quad e_{\mathrm{i}}^{\mathrm{d}} = e_r e_{\mathrm{i}}, \\ &\mu^{\mathrm{d}} = \mu_r \mu, \end{aligned} \tag{7}$$

we obtain

$$\partial_t \rho + \partial_j(\rho u_j) = 0 \tag{8a}$$

$$\partial_t(\rho u_i) + \partial_j(\rho u_i u_j) + \frac{1}{\gamma\, Ma^2}\partial_i p - \frac{1}{Re}\partial_j \sigma_{ij} = \rho f_i \tag{8b}$$

$$\begin{aligned} \partial_t(\rho e) + \partial_j(\rho h u_j) - \frac{\gamma\, Ma^2}{Re}\partial_j(u_i \sigma_{ij}) \\ + \frac{1}{\kappa Re Pr}\partial_j q_j = \gamma Ma^2 \rho f_j u_j, \end{aligned} \tag{8c}$$

where

$$Ma = \frac{V_r}{(\gamma R T_r)^{1/2}}, \qquad Re = \frac{\rho_r V_r L_r}{\mu_r} \tag{9}$$

and

$$\rho h = \rho e + p, \qquad \gamma = \frac{c_p}{c_v}, \qquad \kappa = \frac{R}{c_p}.$$

Other relevant equations in dimensionless form are the equation of state

$$p = \rho T, \tag{10}$$

the definition of the internal energy

$$e = e_{\mathrm{i}} + \frac{\gamma Ma^2}{2} u_k u_k, \qquad e_{\mathrm{i}} = \frac{1-\kappa}{\kappa} T, \tag{11}$$

the constitutive equations

$$\sigma_{ij} = \mu \mathcal{S}_{ij}^d, \qquad q_i = -\mu \partial_i T, \tag{12}$$

with $\mathcal{S}_{ij} = \partial_j u_i + \partial_i u_j$ and $\mathcal{S}_{ij}^d = \mathcal{S}_{ij} - \frac{1}{3}\mathcal{S}_{kk}\delta_{ij}$, and the temperature dependent viscosity $\mu(T) = T^{\alpha}$.

In order to derive the filtered equations for the LES model, an appropriate filter has to be introduced, which will be denoted by the operator $\bar{\cdot}$ and which is assumed to be characterized by a spatial scale Δ. Using an approach that recalls the VMS concept, the precise definition of this operator, as well as of the associated scale, will be built in the numerical DG discretization. Such a definition will be given in section 3; here, we mention that Δ will in

general depend on the local element size and therefore has to be interpreted as a piecewise constant function in space. As customary in compressible LES, see e.g. [19], in order to avoid subgrid terms arising in the continuity equation, we also introduce the Favre filtering operator $\widetilde{\cdot}$, defined implicitly by the Favre decomposition

$$\overline{\rho u_i} = \overline{\rho}\widetilde{u}_i, \qquad \overline{\rho e} = \overline{\rho}\widetilde{e}. \tag{13}$$

Similar decompositions are introduced for the internal energy and the enthalpy

$$\overline{\rho e_{\rm i}} = \overline{\rho}\widetilde{e_{\rm i}}, \qquad \overline{\rho h} = \overline{\rho}\widetilde{h} = \overline{\rho}\widetilde{e} + \overline{p},$$

as well as for the temperature, which, taking into account (10), yields

$$\overline{\rho T} = \overline{\rho}\widetilde{T} = \overline{p}. \tag{14}$$

Equation (11) then implies

$$\overline{\rho}\widetilde{e} = \overline{\rho}\widetilde{e_{\rm i}} + \frac{\gamma Ma^2}{2}\left(\overline{\rho}\widetilde{u}_k\widetilde{u}_k + \tau_{kk}\right), \quad \overline{\rho}\widetilde{e_{\rm i}} = \frac{1-\kappa}{\kappa}\overline{\rho}\widetilde{T}, \tag{15}$$

where, as customary,

$$\tau_{ij} = \overline{\rho u_i u_j} - \overline{\rho}\widetilde{u}_i\widetilde{u}_j. \tag{16}$$

Notice that, from (15), τ_{kk} represents the filtered turbulent kinetic energy. Finally, neglecting the subgrid scale contributions, we introduce a filtered counterpart of (12), namely

$$\widetilde{\sigma}_{ij} = \mu(\widetilde{T})\widetilde{\mathcal{S}}^d_{ij}, \qquad \widetilde{q}_i = -\mu(\widetilde{T})\partial_i\widetilde{T}, \tag{17}$$

with $\widetilde{\mathcal{S}}_{ij} = \partial_j\widetilde{u}_i + \partial_i\widetilde{u}_j$ and $\widetilde{\mathcal{S}}^d_{ij} = \widetilde{\mathcal{S}}_{ij} - \frac{1}{3}\widetilde{\mathcal{S}}_{kk}\delta_{ij}$. It is to be remarked that the filter operators in general do not commute with differential operators. According to a not uncommon practice in LES modeling [46], we will neglect this commutation error. We plan to address this issue in more detail in a future work. An analysis of the terms resulting from non zero commutators between differential operators and projection filters analogous to those we will employ is presented e.g. in [13].

With these definitions, the filtered form of (8) is

$$\partial_t\overline{\rho} + \partial_j(\overline{\rho}\widetilde{u}_j) = 0 \tag{18a}$$

$$\partial_t\left(\overline{\rho}\widetilde{u}_i\right) + \partial_j\left(\overline{\rho}\widetilde{u}_i\widetilde{u}_j\right) + \frac{1}{\gamma\, Ma^2}\partial_i\overline{p} - \frac{1}{Re}\partial_j\widetilde{\sigma}_{ij} = -\partial_j\tau_{ij} - \partial_j\epsilon^{\rm sgs}_{ij} + \overline{\rho}f_i \tag{18b}$$

$$\partial_t\left(\overline{\rho}\widetilde{e}\right) + \partial_j\left(\overline{\rho}\widetilde{h}\widetilde{u}_j\right) - \frac{\gamma\, Ma^2}{Re}\partial_j\left(\widetilde{u}_i\widetilde{\sigma}_{ij}\right) + \frac{1}{\kappa RePr}\partial_j\widetilde{q}_j = -\partial_j\left(\rho h u_j\right)^{\rm sgs} + \frac{\gamma\, Ma^2}{Re}\partial_j\phi^{\rm sgs}_j - \frac{1}{\kappa RePr}\partial_j\theta^{\rm sgs}_j + \gamma Ma^2\overline{\rho}f_j\widetilde{u}_j, \tag{18c}$$

where

$$\epsilon^{\rm sgs}_{ij} = \overline{\sigma}_{ij} - \widetilde{\sigma}_{ij}, \qquad \left(\rho h u_i\right)^{\rm sgs} = \overline{\rho h u_i} - \overline{\rho}\widetilde{h}\widetilde{u}_i,$$
$$\phi^{\rm sgs}_j = \overline{u_i\sigma_{ij}} - \widetilde{u}_i\widetilde{\sigma}_{ij}, \quad \theta^{\rm sgs}_i = \overline{q}_i - \widetilde{q}_i. \tag{19}$$

Based on the analyses presented e.g. in [40] and [57] and on the fact that

$$\overline{\sigma}_{ij} \approx \widetilde{\sigma}_{ij}, \qquad \overline{q}_i \approx \widetilde{q}_i, \tag{20}$$

the term $\partial_j\phi^{\rm sgs}_j$ is considered to be negligible, as well as $\epsilon^{\rm sgs}_{ij}$ and $\theta^{\rm sgs}_j$. To avoid unnecessary complications, and since this is the case for the numerical results considered in this work, we assume in (18) that the forcing $\mathbf{f}$ is uniform in space. Concerning the subgrid enthalpy flux, we proceed as follows. First of all, notice that using (10) and (11), as

well as their filtered counterparts (14) and (15), we have

$$\rho h = \frac{1}{\kappa}\rho T + \frac{\gamma Ma^2}{2}\rho u_k u_k,$$
$$\overline{\rho}\widetilde{h} = \frac{1}{\kappa}\overline{\rho}\widetilde{T} + \frac{\gamma Ma^2}{2}\left(\overline{\rho}\widetilde{u}_k\widetilde{u}_k + \tau_{kk}\right).$$

Introducing now the subgrid heat and turbulent diffusion fluxes

$$Q_i^{\text{sgs}} = \overline{\rho u_i T} - \overline{\rho}\widetilde{u}_i\widetilde{T} = \overline{\rho}\left(\widetilde{u_i T} - \widetilde{u}_i\widetilde{T}\right) \tag{22a}$$
$$J_i^{\text{sgs}} = \overline{\rho u_i u_k u_k} - \overline{\rho}\widetilde{u}_i\widetilde{u}_k\widetilde{u}_k = \overline{\rho}\widetilde{u_i u_k u_k} - \overline{\rho}\widetilde{u}_i\widetilde{u}_k\widetilde{u}_k \tag{22b}$$

we have

$$(\rho h u_i)^{\text{sgs}} = \frac{1}{\kappa}Q_i^{\text{sgs}} + \frac{\gamma Ma^2}{2}\left(J_i^{\text{sgs}} - \tau_{kk}\widetilde{u}_i\right). \tag{23}$$

Notice that, introducing the generalized central moments $\tau(u_i, u_j, u_k)$ as in [20], with

$$\tau(u_i, u_j, u_k) = \overline{\rho}\widetilde{u_i u_j u_k} - \widetilde{u}_i\tau_{jk} - \widetilde{u}_j\tau_{ik} - \widetilde{u}_k\tau_{ij} - \overline{\rho}\widetilde{u}_i\widetilde{u}_j\widetilde{u}_k, \tag{24a}$$

J_i^{sgs} in (22b) can be rewritten as

$$J_i^{\text{sgs}} = \tau(u_i, u_k, u_k) + 2\widetilde{u}_k\tau_{ik} + \widetilde{u}_i\tau_{kk}. \tag{25}$$

Summarizing, given the above approximations and definitions, the filtered equations (18) become

$$\partial_t\overline{\rho} + \partial_j(\overline{\rho}\widetilde{u}_j) = 0 \tag{26a}$$
$$\partial_t\left(\overline{\rho}\widetilde{u}_i\right) + \partial_j\left(\overline{\rho}\widetilde{u}_i\widetilde{u}_j\right) + \frac{1}{\gamma\, Ma^2}\partial_i\overline{p} - \frac{1}{Re}\partial_j\widetilde{\sigma}_{ij} = -\partial_j\tau_{ij} + \overline{\rho}f_i \tag{26b}$$
$$\partial_t\left(\overline{\rho}\widetilde{e}\right) + \partial_j\left(\overline{\rho}\widetilde{h}\widetilde{u}_j\right) - \frac{\gamma\, Ma^2}{Re}\partial_j\left(\widetilde{u}_i\widetilde{\sigma}_{ij}\right) + \frac{1}{\kappa RePr}\partial_j\widetilde{q}_j = -\frac{1}{\kappa}\partial_j Q_j^{\text{sgs}} - \frac{\gamma Ma^2}{2}\partial_j\left(J_j^{\text{sgs}} - \tau_{kk}\widetilde{u}_j\right) + \gamma Ma^2\overline{\rho}f_j\widetilde{u}_j. \tag{26c}$$

2. Subgrid models

We will now introduce the subgrid models used in our LES experiments. Firstly, we will briefly recall the formulation of the classical Smagorinsky subgrid model, which, in spite of its limitations (see e.g. the discussion in [46]), has been applied almost exclusively in the DG-LES models proposed in the literature so far. Moreover, we will discuss the isotropic dynamic model [21], [38], and then an anisotropic subgrid model proposed in [2] and here extended to the compressible case.

2.1. The Smagorinsky model

In a Smagorinsky-type model, the deviatoric part of the subgrid stress tensor τ_{ij} in (26) is modelled by a scalar turbulent viscosity ν^{sgs}, yielding

$$\tau_{ij} - \frac{1}{3}\tau_{kk}\delta_{ij} = -\frac{1}{Re}\overline{\rho}\nu^{\text{sgs}}\widetilde{\mathcal{S}}_{ij}^d, \tag{27a}$$
$$\nu^{\text{sgs}} = Re\, C_S^2\Delta^2|\widetilde{\mathcal{S}}|f_D, \tag{27b}$$

where $C_S = 0.1$ is the Smagorinsky constant, $|\widetilde{\mathcal{S}}|^2 = \frac{1}{2}\widetilde{\mathcal{S}}_{ij}\widetilde{\mathcal{S}}_{ij}$ and Δ is the filter scale introduced in section 1. The Van Driest damping function in (27b) is defined as

$$f_D(y^+) = 1 - \exp\left(-y^+/A\right), \tag{28}$$

where A is a constant and $y^+ = \frac{\rho_r u_\tau^{\text{d}} d_{\text{wall}}^{\text{d}}}{\mu_r}$, with $d_{\text{wall}}^{\text{d}}$ denoting the (dimensional) distance from the wall and u_τ^{d} the (dimensional) friction velocity. The introduction of such a damping function in (27b) is necessary to reduce the scale Δ according to the smaller size of turbulent structures close to the wall and to recover the correct physical trend for the turbulent viscosity, see for instance the discussion in [46]; in the following, the value $A = 25$ is employed. We also notice that the Reynolds number has been included in

the definition of ν^{sgs} so that the corresponding dimensional viscosity can be obtained as $\nu^{\text{sgs,d}} = \frac{\mu_r}{\rho_r}\nu^{\text{sgs}}$.

Concerning the isotropic part of the subgrid stress tensor, some authors [15] have neglected it, considering it negligible with respect to the pressure contribution. Alternatively, following [60], the isotropic components of the subgrid stress tensor can be modelled as:

$$\tau_{kk} = C_I \overline{\rho} \Delta^2 |\widetilde{\mathcal{S}}|^2. \tag{29}$$

Along the lines of [14], the subgrid temperature flux (22a) is assumed to be proportional to the resolved temperature gradient and is modelled with the eddy viscosity model

$$Q_i^{\text{sgs}} = -\frac{Pr}{Pr^{\text{sgs}}} \overline{\rho} \nu^{\text{sgs}} \partial_i \widetilde{T}, \tag{30}$$

where Pr^{sgs} is a subgrid Prandtl number. Notice that the corresponding dimensional flux is $Q_i^{\text{sgs,d}} = q_r Q_i^{\text{sgs}}$.

Finally, concerning J_i^{sgs} in (25), by analogy with RANS models, the term $\tau(u_i, u_j, u_k)$ is neglected (see e.g. [33]), yielding

$$J_i^{\text{sgs}} \approx 2\widetilde{u}_k \tau_{ik} + \widetilde{u}_i \tau_{kk}. \tag{31}$$

2.2. The isotropic dynamic model

We consider now the Germano dynamic procedure proposed in [21] to derive a subgrid-scale closure. In this approach, the constants C_S and C_I of the Smagorinsky model are no more chosen *a priori* for the whole domain, but are dynamically computed in function of the resolved field. The deviatoric part of the subgrid stress tensor is expressed similarly as in (27a)

$$\tau_{ij} - \frac{1}{3}\tau_{kk}\delta_{ij} = -\overline{\rho} C_S \Delta^2 |\widetilde{\mathcal{S}}| \widetilde{\mathcal{S}}_{ij}^d. \tag{32}$$

The dynamic computation of the coefficient C_S relies on the introduction of a test filter operator $\widehat{\cdot}$. As for the filter $\overline{\cdot}$ introduced in section 1, the precise definition of the test filter relies on the numerical discretization and will be given in section 3; here, it will suffice to point out that the test filter is characterized by a spatial scale $\widehat{\Delta}$ larger than the spatial scale Δ associated to $\overline{\cdot}$. The test filter is also associated to a Favre filter, denoted by $\breve{\cdot}$, through the Favre decomposition

$$\widehat{\rho\phi} = \widehat{\rho}\breve{\phi}, \tag{33}$$

where ϕ stands for any of the variables in the equations introduced in section 1. Applying the test filter to the momentum equation (8b) and proceeding as in section 1 we arrive at

$$\partial_t \left(\widehat{\rho}\breve{u}_i\right) + \partial_j \left(\widehat{\rho}\breve{u}_i\breve{u}_j\right) + \frac{1}{\gamma\, Ma^2}\partial_i \widehat{p} - \frac{1}{Re}\partial_j \widehat{\sigma}_{ij} = -\partial_j \left(\widehat{\tau}_{ij} + \mathcal{L}_{ij}\right) \tag{34a}$$

where

$$\mathcal{L}_{ij} = \widehat{\overline{\rho}\widetilde{u}_i\widetilde{u}_j} - \widehat{\overline{\rho}}\breve{\breve{u}}_i\breve{\breve{u}}_j \tag{35}$$

is the Leonard stress tensor. Assuming now that model (32) can be used to represent the right-hand-side of (34a) implies

$$\widehat{\tau}_{ij}^d + \mathcal{L}_{ij}^d = -\widehat{\overline{\rho}}\widehat{\Delta}^2 |\breve{\breve{\mathcal{S}}}| C_S \breve{\breve{\mathcal{S}}}^d{}_{rs}. \tag{36}$$

Substituting (32) for τ_{ij}^d and applying a least square approach [38] provides the required expression

$$C_S = \frac{\mathcal{L}_{ij}^d \mathcal{R}_{ij}}{\mathcal{R}_{kl}\mathcal{R}_{kl}}, \tag{37}$$

where

$$\mathcal{R}_{kl} = \overline{\rho}\widehat{\Delta^2 |\widetilde{\mathcal{S}}| \widetilde{\mathcal{S}}_{kl}^d} - \widehat{\overline{\rho}}\widehat{\Delta}^2 |\breve{\breve{\mathcal{S}}}| \breve{\breve{\mathcal{S}}}^d{}_{kl}. \tag{38}$$

Similarly, the dynamic procedure is applied to the isotropic components of the subgrid stress tensor

$$\tau_{kk} = C_I \overline{\rho} \Delta^2 |\widetilde{\mathcal{S}}|^2. \tag{39}$$

where the C_I coefficient is determined by

$$C_I = \frac{\mathcal{L}_{kk}}{\widehat{\overline{\rho}}\widehat{\Delta}^2 |\breve{\widetilde{\mathcal{S}}}|^2 - \widehat{\overline{\rho}\Delta^2 |\widetilde{\mathcal{S}}|^2}} \tag{40}$$

The approach outlined above has some appealing features that allow to overcome some difficulties of the Smagorinsky model. Firstly, the use of a damping function is not necessary any more to obtain correct results in the wall region [21]. Moreover, while the Smagorinsky model (27) is dissipative by construction, the dynamic procedure allows backscatter, i.e. a positive work done by the subgrid stresses on the mean flow. This is indeed a desirable property of the model, yet one must ensure that the total dissipation, resulting from both the viscous and the subgrid stresses, is positive. This amounts to requiring

$$\frac{1}{Re} \widetilde{\sigma}_{ij} \widetilde{\mathcal{S}}_{ij} - \tau_{ij} \widetilde{\mathcal{S}}_{ij} \geq 0,$$

which can be ensured by introducing a limiting coefficient in (32), so as to obtain

$$\beta = \begin{cases} 1, & \tau_{ij} \widetilde{\mathcal{S}}_{ij} \leq 0 \\ \min\left(1, \frac{1}{Re} \frac{\widetilde{\sigma}_{ij} \widetilde{\mathcal{S}}_{ij}}{\tau_{kl} \widetilde{\mathcal{S}}_{kl}}\right), & \tau_{ij} \widetilde{\mathcal{S}}_{ij} > 0. \end{cases} \tag{41}$$

Having defined the subgrid stresses, let us consider now the subgrid terms in the energy equation, namely $\mathbf{Q}^{\text{sgs}}$ and $\mathbf{J}^{\text{sgs}}$. Here, we propose to treat both of them within the same dynamic framework used for the subgrid stresses. Concerning the subgrid heat flux, we let

$$Q_i^{\text{sgs}} = -\overline{\rho} \Delta^2 |\widetilde{\mathcal{S}}| C_Q \partial_i \widetilde{T}, \tag{42}$$

where the coefficient C_Q can be computed locally by the dynamic procedure. To this aim, we define the temperature Leonard flux

$$\mathcal{L}_i^Q = \widehat{\overline{\rho} \widetilde{u}_i \widetilde{T}} - \widehat{\overline{\rho}} \breve{\widetilde{u}}_i \breve{\widetilde{T}}, \tag{43}$$

we apply the test filter to the energy equation (8c) and we observe that, thanks to the similarity hypothesis, model (42) should be also applied in the resulting equation, so that

$$\widehat{Q}_i^{\text{sgs}} + \mathcal{L}_i^Q = -\widehat{\overline{\rho}} \widehat{\Delta}^2 |\breve{\widetilde{\mathcal{S}}}| C_Q \partial_i \breve{\widetilde{T}}. \tag{44}$$

Substituting (42) for $\widehat{Q}_i^{\text{sgs}}$, applying the least squares method yields

$$C_Q = \frac{\mathcal{L}_i^Q \mathcal{R}_i^Q}{\mathcal{R}_k^Q \mathcal{R}_k^Q}, \tag{45}$$

where

$$\mathcal{R}_i^Q = \widehat{\overline{\rho} \Delta^2 |\widetilde{\mathcal{S}}|} \partial_i \widetilde{T} - \widehat{\overline{\rho}} \widehat{\Delta}^2 |\breve{\widetilde{\mathcal{S}}}| \partial_i \breve{\widetilde{T}}. \tag{46}$$

Contrary to what is done in the Smagorinsky model, we do not neglect the term $\tau(u_i, u_k, u_k)$ in (25), but instead adopt a scale similarity model as in [40] where such term is approximated as a subgrid kinetic energy flux

$$\tau(u_i, u_k, u_k) \approx \overline{\rho} \widetilde{u_i u_k u_k} - \overline{\rho} \widetilde{u}_i \widetilde{u_k u_k}. \tag{47}$$

Coherently with the other subgrid terms, $\tau(u_i, u_k, u_k)$ can now be modeled as a function of the gradient of the resolved kinetic energy, letting

$$\tau(u_i, u_k, u_k) = -\overline{\rho} \Delta^2 |\widetilde{\mathcal{S}}| C_J \partial_i \left(\frac{1}{2} \widetilde{u}_k \widetilde{u}_k \right). \tag{48}$$

Introducing the kinetic energy Leonard flux

$$\mathcal{L}_i^J = \widehat{\overline{\rho} \widetilde{u}_i \widetilde{u}_k \widetilde{u}_k} - \widehat{\overline{\rho}} \breve{\widetilde{u}}_i \breve{\widetilde{u}}_k \breve{\widetilde{u}}_k \tag{49}$$

and proceeding exactly as for the previous terms we arrive

at

$$C_J = \frac{\mathcal{L}_i^J \mathcal{R}_i^J}{\mathcal{R}_k^J \mathcal{R}_k^J}, \tag{50}$$

where

$$\mathcal{R}_i^J = \overline{\rho}\Delta^2 \widetilde{|\mathcal{S}|\partial_i}\left(\frac{1}{2}\widetilde{u}_k\widetilde{u}_k\right) - \widehat{\overline{\rho}}\widehat{\Delta}^2 \breve{|\mathcal{S}|}\partial_i\left(\frac{1}{2}\breve{\widetilde{u}}_k\breve{\widetilde{u}}_k\right). \tag{51}$$

To avoid numerical instabilities, all the model coefficients are assumed to be averaged over each element, while they are not averaged in time. This provides a local definition for such coefficients that does not rely on the existence of any homogeneity direction in space or quasi-stationary hypothesis in time [46].

2.3. The anisotropic dynamic model

We consider now the dynamic, anisotropic subgrid model proposed in [2], which is extended here to the compressible case. This approach has the goal of removing the limitation related to the previously introduced isotropic models, in particular the alignment of the subgrid flux tensors with the gradients of the corresponding quantities. The subgrid tensor alignment is removed by generalizing the proportionality relations such as (27a) introducing proportionality parameters which are tensors rather than scalar quantities.

More specifically, the subgrid stress tensor τ_{ij} is assumed proportional to the strain rate tensor through a fourth order symmetric tensor as follows

$$\tau_{ij} = -\overline{\rho}\Delta^2 |\widetilde{\mathcal{S}}| \mathcal{B}_{ijrs} \widetilde{\mathcal{S}}_{rs}. \tag{52}$$

To compute dynamically the tensor $\mathcal{B}_{ijrs}$, let us first observe that a generic, symmetric fourth order tensor can be represented as

$$\mathcal{B}_{ijrs} = \sum_{\alpha,\beta=1}^{3} \mathcal{C}_{\alpha\beta} a_{i\alpha} a_{j\beta} a_{r\alpha} a_{s\beta}, \tag{53}$$

where a_{ij} is a rotation tensor (i.e. an orthogonal matrix with positive determinant) and $\mathcal{C}_{\alpha\beta}$ is a second order, symmetric tensor; (53) is of course a generalization of the orthogonal diagonalization for symmetric second order tensors. This observation allows us to define the following algorithm:

1. choose a rotation tensor a_{ij}
2. compute with the Germano dynamic procedure the six components of $\mathcal{C}_{\alpha\beta}$
3. define $\mathcal{B}_{ijrs}$ using (53), thereby completely determining the subgrid flux (52).

The anisotropic model does not prescribe how to choose the tensor a_{ij}, which in principle can be any rotation tensor, possibly varying in space and time. The values of the components $\mathcal{C}_{\alpha\beta}$ computed with the dynamic procedure depend on the chosen tensor, and different choices for a_{ij} result in general in different subgrid fluxes. Many different choices have been proposed in the past, essentially trying to identify at each position three directions intrinsically related to the flow configuration; examples are a vorticity aligned basis, the eigenvectors of the velocity strain rate, or the eigenvectors of the Leonard stresses [1], [2], [22]. In our experience, however, the results of the simulations do not appear to have a strong dependency on the choice of a_{ij}. In the present work, the components of a_{ij} are identified with those of the canonic Cartesian basis of the three dimensional space, i.e. $a_{ij} = \delta_{ij}$, essentially because of the simplicity of this choice and because the results presented here are obtained for the channel flow problem, for which the coordinate axes do identify significant directions for the problem, namely the longitudinal, transversal and spanwise directions.

As in section 2.2, the dynamic computation of the components $\mathcal{C}_{\alpha\beta}$ relies on the assumption that the model (52)

can be used to represent the right-hand-side of (34a):

$$\widehat{\tau}_{ij} + \mathcal{L}_{ij} = -\widehat{\overline{\rho}\Delta^2}|\breve{\widetilde{\mathcal{S}}}|\mathcal{B}_{ijrs}\breve{\widetilde{\mathcal{S}}}_{rs}. \tag{54}$$

Now, multiplying (54) by $a_{i\alpha}a_{j\beta}$ and summing over i, j, using the orthogonality of the rotation tensor,

$$a_{i\alpha}a_{j\beta}\left(\widehat{\tau}_{ij} + \mathcal{L}_{ij}\right) = -\widehat{\overline{\rho}\Delta^2}|\breve{\widetilde{\mathcal{S}}}|\mathcal{C}_{\alpha\beta}a_{r\alpha}a_{s\beta}\breve{\widetilde{\mathcal{S}}}_{rs},$$

substituting (52) for τ_{ij} and solving for $\mathcal{C}_{\alpha\beta}$ provide the required expression

$$\mathcal{C}_{\alpha\beta} = \frac{a_{i\alpha}\mathcal{L}_{ij}a_{j\beta}}{a_{r\alpha}a_{s\beta}\left(\widehat{\overline{\rho}\Delta^2|\widetilde{\mathcal{S}}|\widetilde{\mathcal{S}}_{rs}} - \widehat{\overline{\rho}\Delta^2}|\breve{\widetilde{\mathcal{S}}}|\breve{\widetilde{\mathcal{S}}}_{rs}\right)}. \tag{55}$$

Since in this work we assume $a_{ij} = \delta_{ij}$ we immediately have

$$\mathcal{C}_{ij} = \frac{\mathcal{L}_{ij}}{\left(\widehat{\overline{\rho}\Delta^2|\widetilde{\mathcal{S}}|\widetilde{\mathcal{S}}_{ij}} - \widehat{\overline{\rho}\Delta^2}|\breve{\widetilde{\mathcal{S}}}|\breve{\widetilde{\mathcal{S}}}_{ij}\right)} \tag{56}$$

and

$$\tau_{ij} = -\overline{\rho}\Delta^2|\widetilde{\mathcal{S}}|\mathcal{C}_{ij}\widetilde{\mathcal{S}}_{ij}. \tag{57}$$

Notice that, as an exception to the convention generally used in this paper, no summation over repeated indices is implied in the above formula. By the approach outlined above, the deviatoric and isotropic parts of the subgrid stress tensor are modelled together, without splitting the two contributions. As in section 2.2, the coefficients $\mathcal{C}_{ij}$ are assumed to be averaged over each element and a limiting coefficient is introduced to ensure positive total dissipation.

Concerning the subgrid heat flux, we let

$$Q_i^{\text{sgs}} = -\overline{\rho}\Delta^2|\widetilde{\mathcal{S}}|\mathcal{B}_{ir}^Q\partial_r\widetilde{T}, \tag{58}$$

where $\mathcal{B}_{ir}^Q$ is a symmetric tensor. Assuming that $\mathcal{B}_{ir}^Q$ is diagonal in the reference defined by the rotation tensor a we have

$$\mathcal{B}_{ir}^Q = \sum_{\alpha=1}^{3}\mathcal{C}_\alpha^Q a_{i\alpha}a_{r\alpha}, \tag{59}$$

where the three coefficients $\mathcal{C}_\alpha^Q$ can be computed locally by the dynamic procedure. As usual, model (58) should be also applied to model the right-and-side of the test filtered energy equation:

$$\widehat{Q}_i^{\text{sgs}} + \mathcal{L}_i^Q = -\widehat{\overline{\rho}\Delta^2}|\breve{\widetilde{\mathcal{S}}}|\mathcal{B}_{ir}^Q\partial_r\breve{\widetilde{T}}. \tag{60}$$

Substituting (58) and (59) for $\widehat{Q}_i^{\text{sgs}}$, multiplying by $a_{i\alpha}$, summing over i and solving for $\mathcal{C}_\alpha$ yields

$$\mathcal{C}_\alpha^Q = \frac{a_{i\alpha}\mathcal{L}_i^Q}{a_{r\alpha}\left(\widehat{\overline{\rho}\Delta^2|\widetilde{\mathcal{S}}|}\partial_r\widetilde{T} - \widehat{\overline{\rho}\Delta^2}|\breve{\widetilde{\mathcal{S}}}|\partial_r\breve{\widetilde{T}}\right)}. \tag{61}$$

The anisotropic dynamic procedure is also applied to model the subgrid kinetic energy flux

$$\tau(u_i, u_k, u_k) \approx \overline{\rho}\widetilde{u_i u_k u_k} - \overline{\rho}\widetilde{u}_i\widetilde{u_k u_k}. \tag{62}$$

Coherently with the other subgrid terms, a symmetric tensor $\mathcal{B}_{ir}^J$ is defined

$$\mathcal{B}_{ir}^J = \sum_{\alpha=1}^{3}\mathcal{C}_\alpha^J a_{i\alpha}a_{r\alpha}, \tag{63}$$

letting

$$\tau(u_i, u_k, u_k) = -\overline{\rho}\Delta^2|\widetilde{\mathcal{S}}|\mathcal{B}_{ir}^J\partial_r\left(\frac{1}{2}\widetilde{u}_k\widetilde{u}_k\right). \tag{64}$$

Proceeding exactly as for the previous terms we arrive at

$$\mathcal{C}_\alpha^J = a_{i\alpha}\mathcal{L}_i^J/\mathcal{M}_\alpha, \tag{65}$$

where

$$\mathcal{M}_\alpha = a_{r\alpha}\left(\overline{\rho}\Delta^2|\widetilde{\mathcal{S}}|\widehat{\partial_r\left(\frac{1}{2}\widetilde{u}_k\widetilde{u}_k\right)} - \widehat{\overline{\rho}\Delta^2}|\breve{\widetilde{\mathcal{S}}}|\partial_r\left(\frac{1}{2}\breve{\widetilde{u}}_k\breve{\widetilde{u}}_k\right)\right).$$

3. Discretization and filtering

The equations introduced in section 1, including the subgrid scale models defined in section 2, will be discretized in space by a discontinous finite element method. The DG approach employed for the spatial discretization is analogous to that described in [23] and relies on the so called Local Discontinuous Galerkin (LDG) method, see e.g. [5], [4], [7], [8], for the approximation of the second order viscous terms. We provide here a concise description of the method; a more detailed description can be found in [39].

In the LDG method, (26) is rewritten introducing an auxiliary variable $\boldsymbol{\mathcal{G}}$, so that

$$\begin{aligned} \partial_t\mathbf{U} + \nabla\cdot\mathbf{F}^{\mathrm{c}}(\mathbf{U}) &= \nabla\cdot\mathbf{F}^{\mathrm{v}}(\mathbf{U},\boldsymbol{\mathcal{G}}) \\ &- \nabla\cdot\mathbf{F}^{\mathrm{sgs}}(\mathbf{U},\boldsymbol{\mathcal{G}}) + \mathbf{S} \qquad (66)\\ \boldsymbol{\mathcal{G}} &- \nabla\boldsymbol{\varphi} = 0, \end{aligned}$$

where $\mathbf{U} = [\overline{\rho}\,, \overline{\rho}\widetilde{\mathbf{u}}^T, \overline{\rho}\widetilde{e}]^T$ are the prognostic variables, $\boldsymbol{\varphi} = [\widetilde{\mathbf{u}}^T, \widetilde{T}]^T$ are the variables whose gradients enter the viscous fluxes (17) as well as the turbulent ones and $\mathbf{S}$ represents the source terms. In (66), the following compact notation for the fluxes is been used:

$$\mathbf{F}^{\mathrm{c}} = \begin{bmatrix} \overline{\rho}\widetilde{\mathbf{u}} \\ \overline{\rho}\widetilde{\mathbf{u}}\otimes\widetilde{\mathbf{u}} + \frac{1}{\gamma Ma^2}\overline{p}\mathcal{I} \\ \overline{\rho}\widetilde{h}\widetilde{\mathbf{u}} \end{bmatrix},$$

$$\mathbf{F}^{\mathrm{v}} = \begin{bmatrix} 0 \\ \frac{1}{Re}\widetilde{\sigma} \\ \frac{\gamma Ma^2}{Re}\widetilde{\mathbf{u}}^T\widetilde{\sigma} - \frac{1}{\kappa RePr}\widetilde{\mathbf{q}} \end{bmatrix}$$

and

$$\mathbf{F}^{\mathrm{sgs}} = \begin{bmatrix} 0 \\ \tau \\ \frac{1}{\kappa}\mathbf{Q}^{\mathrm{sgs}} + \frac{\gamma Ma^2}{2}\left(\mathbf{J}^{\mathrm{sgs}} - \tau_{kk}\widetilde{\mathbf{u}}\right) \end{bmatrix},$$

$$\mathbf{S} = \begin{bmatrix} 0 \\ \overline{\rho}\mathbf{f} \\ \gamma Ma^2\overline{\rho}\mathbf{f}\cdot\widetilde{\mathbf{u}} \end{bmatrix}.$$

Here, τ, $\mathbf{Q}^{\mathrm{sgs}}$ and $\mathbf{J}^{\mathrm{sgs}}$ are given by (27), (30) and (31), respectively, for the Smagorinsky model. For the isotropic dynamic model, they are given by (32), including the limiting coefficient (41), (42) and (25) together with (47), while for the anisotropic dynamic model they are given by the corresponding expressions (52), (58) and (62).

The discretization is then obtained by first introducing a space discretization and then using a time integrator to advance in time the numerical solution. For the time integration, we consider here the fourth order, five stages, Strongly Stability Preserving Runge–Kutta method (SSPRK) proposed in [52]. To define the space discretization, we first introduce a tessellation $\mathcal{T}_h$ of Ω into tetrahedral elements K such that $\Omega = \bigcup_{K\in\mathcal{T}_h} K$ and $K\cap K' = \emptyset$ and define the finite element space

$$\mathcal{V}_h = \left\{v_h \in L^2(\Omega) : v_h|_K \in \mathbb{P}^q(K),\ \forall K\in\mathcal{T}_h\right\}, \qquad (67)$$

where q is a nonnegative integer and $\mathbb{P}^q(K)$ denotes the space of polynomial functions of total degree at most q on K. Notice that, while only conforming meshes have been employed in this work, any DG formulation also extends seamlessly to non conforming meshes. Furthermore, although the same polynomial degree q has been employed here for all elements, degree adaptivity techniques can be easily implemented in the same framework, see e.g. [53], [54]. For each element, the outward unit normal on ∂K

will be denoted by $\mathbf{n}_{\partial K}$. The numerical solution is now defined as $(\mathbf{U}_h, \boldsymbol{\mathcal{G}}_h) \in (\,(\mathcal{V}_h)^5\,,\,(\mathcal{V}_h)^{4\times 3}\,)$ such that, $\forall K \in \mathcal{T}_h$, $\forall v_h \in \mathcal{V}_h$, $\forall \mathbf{r}_h \in (\mathcal{V}_h)^3$,

$$\frac{d}{dt}\int_K \mathbf{U}_h v_h \, d\mathbf{x} - \int_K \mathbf{F}(\mathbf{U}_h, \boldsymbol{\mathcal{G}}_h)\cdot\nabla v_h \, d\mathbf{x} + \int_{\partial K} \widehat{\mathbf{F}}(\mathbf{U}_h, \boldsymbol{\mathcal{G}}_h)\cdot \mathbf{n}_{\partial K} v_h \, d\sigma = \int_K \mathbf{S} v_h \, d\mathbf{x}, \tag{68a}$$

$$\int_K \boldsymbol{\mathcal{G}}_h \cdot \mathbf{r}_h \, d\mathbf{x} + \int_K \boldsymbol{\varphi}_h \nabla\cdot \mathbf{r}_h \, d\mathbf{x} - \int_{\partial K} \widehat{\boldsymbol{\varphi}}\mathbf{n}_{\partial K}\cdot \mathbf{r}_h \, d\sigma = 0, \tag{68b}$$

where $\mathbf{U}_h = [\rho_h\,, \rho_h \mathbf{u}_h\,, \rho_h e_h]^T$, $\boldsymbol{\varphi}_h = [\mathbf{u}_h\,, T_h]^T$, $\mathbf{F} = \mathbf{F}^{\mathrm{c}} - \mathbf{F}^{\mathrm{v}} + \mathbf{F}^{\mathrm{sgs}}$, and $\widehat{\mathbf{F}}$, $\widehat{\boldsymbol{\varphi}}$ denote the so-called *numerical fluxes*. To understand the role of these fluxes, notice that (68) can be regarded as a weak formulation of (67) on the single element K with weakly imposed boundary conditions $\widehat{\mathbf{F}}$, $\widehat{\boldsymbol{\varphi}}$ on ∂K. Hence, the numerical fluxes are responsible for the coupling among the different elements in $\mathcal{T}_h$. In this work we employ the Rusanov flux for $\widehat{\mathbf{F}}$ and the centered flux for $\widehat{\boldsymbol{\varphi}}$; the detailed definitions can be found, for instance, in [23]. To complete the definition of the space discretization, we mention that, on each element, the unknowns are expressed in terms of an orthogonal polynomial basis, yielding what is commonly called a modal DG formulation, and that all the integrals are evaluated using quadrature formulae from [12] which are exact for polynomial orders up to $2q$. This results in a diagonal mass matrix in the time derivative term of (68) and simplifies the computation of L^2 projections to be introduced shortly in connection with the LES filters.

Having defined the general structure of the discretized problem, we turn now to the definition of the filter operators $\bar{\cdot}$ and $\widehat{\cdot}$, introduced in sections 1 and 2.3, respectively, with the associated Favre decompositions. We proceed here along the lines proposed e.g. in [10], [11], [13], defining the filter operators in terms of appropriate L^2 projectors. Given a subspace $\mathcal{V} \subset L^2(\Omega)$, let $\Pi_{\mathcal{V}} : L^2(\Omega) \to \mathcal{V}$ be the associated projector defined by

$$\int_\Omega \Pi_{\mathcal{V}} u \, v \, d\mathbf{x} = \int_\Omega u \, v \, d\mathbf{x}, \qquad \forall u, v \in \mathcal{V},$$

where the integrals are evaluated with the same quadrature rule used in (68). For $v \in L^2(\Omega)$, the filter $\bar{\cdot}$ is now defined by

$$\overline{v} = \Pi_{\mathcal{V}_h} v. \tag{69}$$

Notice that the application of this filter is built in the discretization process and equivalent to it. Therefore, once the discretization of equations (66) has been performed, only $\bar{\cdot}$ filtered quantities are computed by the model. To define the test filter, we then introduce

$$\widehat{\mathcal{V}}_h = \left\{ v_h \in L^2(\Omega) : v_h|_K \in \mathbb{P}^{\widehat{q}}(K),\, \forall K \in \mathcal{T}_h \right\}, \tag{70}$$

where $0 \le \widehat{q} < q$, and we let, for $v \in L^2(\Omega)$,

$$\widehat{v} = \Pi_{\widehat{\mathcal{V}}_h} v. \tag{71}$$

By our previous identification of the $\bar{\cdot}$ filter and the discretization, the quantities $\overline{\rho}$, $\overline{\rho\widetilde{\mathbf{u}}}$ and $\overline{\rho\widetilde{e}}$ can be identified with ρ_h, $\rho_h\mathbf{u}_h$ and $\rho_h e_h$, respectively. Therefore, they belong to $\mathcal{V}_h$, for which an orthogonal basis is employed by the numerical method. As a result, the computation of $\widehat{\rho_h}$, $\widehat{\rho_h\mathbf{u}_h}$ and $\widehat{\rho_h e_h}$ is straightforward and reduces to zeroing the last coefficients in the local expansion. Assuming that the analytic solution is defined in some infinite dimensional subspace of L^2, heuristically, $\mathcal{V}_h \subset L^2$ is associated to the scales which are represented by the model, while $\widehat{\mathcal{V}}_h \subset \mathcal{V}_h \subset L^2$ is associated to the spatial scales well re-

solved by the numerical approximation. A similar concept of *believable scales* was introduced in [35] in the framework of a global spectral transform model for numerical weather prediction.

The Favre filters associated to (69) and (71) are defined by imposing pointwise the conditions (13)-(17) and (33), respectively. Notice that, as a result, for a generic quantity φ the filtered counterpart $\widetilde{\varphi}$ is not, in general, a polynomial but a rational function. All the remaining quantities in (35), (55), (43), (61), (49) and (65) where the test filter appears are computed using (71) and the same quadrature rule used in (68). We also remark that these filters do not commute with the differentiation operators. As previously remarked in section 1, the commutation error will be neglected here.

Finally, we remark that using (55), (61) and (65), the dynamic coefficients C_S, C_I, C_Q, C_J, $\mathcal{C}_{\alpha\beta}$, $\mathcal{C}_\alpha^Q$ and $\mathcal{C}_\alpha^J$ can be computed as functions of space. Substituting these functions directly into the subgrid dynamical models, however, would result in diffusive terms with (possibly) highly irregular diffusion coefficients, which would represent a serious obstacle for a high-order numerical discretization. For this reason, the dynamic coefficients are first averaged over each element and then used in the corresponding subgrid models. This is similar to what is often done in the context of dynamic LES models, where the dynamic coefficients are averaged in space and in time over some homogeneity direction or some local control volume, see e.g. [21], [59], [62]. The proposed approach has the advantage that the average is computed directly on each element of the computational mesh and does not require choosing any special averaging direction. In our implementation, the dynamic coefficients are updated at each Runge–Kutta stage. An alternative approach where they are updated only once for each time-step or for each fixed number of time-steps could be considered, in order to reduce the computational cost. Another important point is choosing the spatial scales Δ and $\widehat{\Delta}$ associated with the two filters (69) and (71). This can be done by dividing the element diameter by the cubic root (or, in two dimensions, the square root) of the number of degrees of freedom of $\mathbb{P}^q(K)$, for Δ, and $\widehat{\mathbb{P}^q}(K)$, for $\widehat{\Delta}$. As anticipated, this leads to space scales which are piecewise constant on $\mathcal{T}_h$. A more precise definition is given in section 4, where we introduce a scaling coefficient which accounts for the mesh anisotropy.

4. Numerical results

4.1. Plane channel flow simulations

In order to compare the performance of the described Smagorinsky, isotropic and anisotropic dynamic models, we have computed a typical LES benchmark for compressible, periodic, plane channel flow at Mach numbers $Ma = 0.2, 0.7$ and 1.5, respectively. The results obtained are compared here with the data from the incompressible numerical simulation of Moser et al. (MKM) [43] for $Ma = 0.2$, with the simulation of Wei and Pollard (WP) [58] for $Ma = 0.7$, and finally with the results presented by Coleman et al. (CKM) [9] for the supersonic case at $Ma = 1.5$.

All the computations were performed using the `FEMilaro` finite element library [16], a FORTRAN/MPI library which, exploiting modern FORTRAN features, aims at providing a flexible environment for the development and testing of new finite element formulations, and which is publicly available under GPL license. In this implementation, the computational cost of the dynamic models was comparable. Indeed, using the same configuration and parallel ma-

chine, the average wall clock times per time step needed by the isotropic and anisotropic dynamic models were 26% and 34% larger, respectively, than that of the Smagorinsky model.

The computational domain Ω^{d} is a box of dimensions L_x^{d}, L_y^{d}, L_z^{d} in dimensional units, that is aligned with a reference frame such that x^{d} represents the streamwise axis, y^{d} the wall normal and z^{d} the spanwise axis. We also introduce $d^{\mathrm{d}} = L_y^d/2$, the half height of the channel. The reference quantities are chosen as follows $\rho_r = \rho_{\mathrm{b}}^{\mathrm{d}}$, $L_r = d^{\mathrm{d}}$, $V_r = U_{\mathrm{b}}^{\mathrm{d}}$, $T_r = T_{\mathrm{w}}^{\mathrm{d}}$, $\mu_r = \mu_{\mathrm{w}}^{\mathrm{d}}$, where $\rho_{\mathrm{b}}^{\mathrm{d}}$ and $U_{\mathrm{b}}^{\mathrm{d}}$ are the bulk density and the target bulk velocity, respectively, and $T_{\mathrm{w}}^{\mathrm{d}}$ is the wall temperature. According to (6), this implies that $\mu_r = \mu^{\mathrm{d}}(T_{\mathrm{w}}^{\mathrm{d}}) = \mu_{\mathrm{w}}^{\mathrm{d}}$, i.e. the viscosity of the fluid at the wall.

In dimensionless units we let $L_x = 4\pi$, $L_y = 2$ and $L_z = 2\pi$ for all the computations, except the cases with $Ma = 0.2$ where we choose $L_x = 2\pi$; the resulting domain is thus $\Omega = [0\,, 4\pi] \times [-1\,, 1] \times [0\,, 2\pi]$, or $\Omega = [0\,, 2\pi] \times [-1\,, 1] \times [0\,, 2\pi]$ for $Ma = 0.2$. Isothermal, no-slip boundary conditions are imposed for $y = \pm 1$, i.e. $T = 1$ and $\mathbf{u} = 0$, while periodic conditions are applied in the streamwise and spanwise directions. The initial condition is represented by a laminar Poiseuille profile $u_x = \frac{3}{4}(1-y^2)$, with $\rho = 1$ and $T = 1$. A random perturbation of amplitude $a = 0.1$ is added to the initial velocity, while no perturbations are added to ρ and T. The perturbation of the $(i+1)$-th velocity component is evaluated at each quadrature node by scaling the i-th coordinate of the node to obtain $\xi^{(0)} \in (0\,, 1)$, computing 20 iterations of the logistic map $\xi^{(k+1)} = 3.999\,\xi^{(k)}(1 - \xi^{(k)})$ and projecting the resulting values, which turn out to be uncorrelated in space, on the local polynomial space; this provides a simple, deterministic and portable way to define a random perturbation of the velocity with zero divergence. The value $U_{\mathrm{b}}^{\mathrm{d}}$ is, by definition, the desired bulk velocity; the flow velocity, however, is the result of the balance between the external forcing and the dissipative terms, so that it can not be easily fixed *a priori*. To ensure that the obtained bulk velocity coincides with the prescribed value, as well as to preserve the homogeneity of the flow in the directions parallel to the wall, a uniform in space body force is included along the streamwise direction, defined by

$$f_x(t) = -\frac{1}{L_y L_z}\left[\alpha_1\left(Q(t) - Q_0\right) + \alpha_2 \int_0^t \left(Q(s) - Q_0\right) ds\right],$$

where $Q(t) = \int_\Omega \rho(t) u_x(t) d\mathbf{x}/L_x$ is the instantaneous flow rate and $Q_0 = L_y L_z$ is the flow rate corresponding to the desired bulk velocity. A sufficiently rapid convergence toward the value Q_0 has been observed by taking $\alpha_1 = 0.1$, $\alpha_2 = 0.5$. The bulk Reynolds and Mach numbers, defined as

$$Re_{\mathrm{b}} = \frac{\rho_{\mathrm{b}}^{\mathrm{d}} U_{\mathrm{b}}^{\mathrm{d}} d^{\mathrm{d}}}{\mu_{\mathrm{w}}^{\mathrm{d}}}, \qquad Ma_{\mathrm{b}} = \frac{U_{\mathrm{b}}^{\mathrm{d}}}{\sqrt{\gamma R T_{\mathrm{w}}^{\mathrm{d}}}},$$

are imposed *a priori*, while the wall shear stress τ_{w}, the friction Reynolds number Re_τ and the skin friction velocity u_τ, defined as

$$\tau_{\mathrm{w}} = \mu_{\mathrm{w}}(\partial_y < u >)_{\mathrm{w}}, \quad Re_\tau = \sqrt{\rho_{\mathrm{w}} Re_{\mathrm{b}} \frac{\tau_{\mathrm{w}}}{\mu_{\mathrm{w}}}},$$

$$u_\tau = \frac{Re_\tau}{Re_{\mathrm{b}} \rho_{\mathrm{w}}}$$

are computed *a posteriori* for each simulation.

The turbulent regime is then characterized by the wall shear stress, the skin friction velocity and the friction Reynolds number

$$\tau_{\mathrm{w}}^{\mathrm{d}} = \mu_{\mathrm{w}}^{\mathrm{d}} \left(\partial_{y^{\mathrm{d}}} < u^{\mathrm{d}} >\right)_{\mathrm{w}}, \quad u_\tau^{\mathrm{d}} = \sqrt{\frac{\tau_{\mathrm{w}}^{\mathrm{d}}}{\rho_{\mathrm{w}}^{\mathrm{d}}}}, \quad Re_\tau^{\mathrm{d}} = \frac{\rho_{\mathrm{w}}^{\mathrm{d}} u_\tau^{\mathrm{d}}}{\mu_{\mathrm{w}}^{\mathrm{d}}},$$

which can be expressed in terms of the dimensionless vari-

ables as

$$\tau_{\rm w} = \left(\partial_y < u >\right)_{\rm w}, \quad u_\tau = \sqrt{\frac{1}{Re_{\rm b}}\frac{\tau_{\rm w}}{\rho_{\rm w}}}, \quad Re_\tau = Re_{\rm b}\rho_{\rm w}u_\tau.$$

Such quantities are computed *a posteriori* for each simulation.

The computational mesh employed is obtained by a structured mesh with $N_x = 16$ ($N_x = 8$ for $Ma = 0.2$), $N_y = 16$, $N_z = 12$ hexahedra in the x, y, z directions, respectively, each of which is then split into $N_t = 6$ tetrahedral elements. While uniform in the x, z directions, the hexahedral mesh is not uniform in the y direction, where the $y = const$ planes are given by

$$y_j = -\frac{\tanh\left(\omega\left(1 - 2j/N_y\right)\right)}{\tanh\left(\omega\right)} \quad \text{for} \quad j = 0, \ldots, N_y. \quad (72)$$

The value of the parameter ω is chosen in order to ensure a sufficient resolution of the boundary layer, as we now illustrate. The polynomial degree for $\mathcal{V}_h$ is $q = 4$, resulting in $N_q = 35$ degrees of freedom in each element. Hence, we can define an equivalent grid spacing

$$\Delta_{x,z} = \frac{L_{x,z}}{N_{x,z}\sqrt[3]{N_t N_q}} \qquad \Delta_{y_i} = \frac{y_i - y_{i-1}}{\sqrt[3]{N_t N_q}},$$

and, in wall units, $\Delta_i^+ = Re_\tau \Delta_i$, for $i = x, y, z$. Using the skin friction Reynolds number of the corresponding DNS, we can now determine $\Delta_{y_1} = \Delta_{y_{min}} = Re_\tau^{-1}\Delta_{y_{min}}^+$ requiring that several points are located at a distance from the wall $y^+ < 5$, so that the boundary layer is well resolved. This in turn determines ω in (72). Here, we take $\omega = 2.0826$. The parameters for the three cases considered here, computed using the skin friction Reynolds number of the corresponding DNS, are summarized in Table 1, along with the comparison test cases presented in literature.

The grid filter scales Δ and $\widehat{\Delta}$ which appear in the models described in Section 2 are defined as piecewise constant values on each element, and are denoted by $\Delta(K)$ and $\widehat{\Delta}(K)$. Such quantities can be estimated as suggested by [50] for strongly anisotropic meshes. For each tetrahedral element K, let us first denote by $\Delta^{(i)}(K)$ the dimensions of the hexahedron from which the element was obtained, for $i = x, y, z$. Then, for each element K, we define

$$a_l = \frac{\Delta^{(l)}(K)}{\max_i \Delta^{(i)}(K)} \qquad a_k = \frac{\Delta^{(k)}(K)}{\max_i \Delta^{(i)}(K)}$$

where l and k are the directions in which the maximum is not attained, and

$$f = \cosh\sqrt{\frac{4}{27}\left[(\ln a_l)^2 - \ln a_l \ln a_k + (\ln a_k)^2\right]} \quad (73a)$$

$$\Delta(K) = \left(\frac{\prod_{i=1}^3 \Delta^{(i)}(K)}{N_q}\right)^{1/3} f. \quad (73b)$$

The test filter scale $\widehat{\Delta}(K)$ is defined analogously, considering that the polynomial degree for $\widehat{\mathcal{V}}_h$ is $\widehat{q} = 2$, resulting in $N_{\widehat{q}} = 10$ degrees of freedom in each element.

For the Smagorinsky-type model, a test with $C_I = 0.01$ seemed to enhance the dissipative behaviour of the model, so that all the results presented in the following have been computed with $C_I = 0$, as in [15] and [37], where the isotropic contribution is neglected.

After the statistical steady state was reached at time $t_{\rm st}$, the simulations were continued for a dimensionless time $t_{\rm av}$ larger or equal than 90 dimensionless time units, in order to compute all the relevant statistics and to verify time invariance of the mean profiles. The statistics were then computed averaging on the element faces parallel to the walls, introducing, for a generic quantity φ, the space-

	Moser et al. (MKM)	Wei and Pollard (WP)	Coleman et al. (CKM)	Present Ma=0.2 (Ma02)	Present Ma=0.7 (Ma07)	Present Ma=1.5 (Ma15)
$Ma_{\rm b}$	—	0.7	1.5	0.2	0.7	1.5
$Re_{\rm b}$	2800	2795	3000	2800	2795	3000
L_x	4π	12	4π	2π	4π	4π
L_z	$\frac{4}{3}\pi$	6	$\frac{4}{3}\pi$	$\frac{4}{3}\pi$	$\frac{4}{3}\pi$	$\frac{4}{3}\pi$
Δ_x^+	17.7	4.89	19	23	24	29
Δ_z+	5.9	4.89	12	10	11	13
$\Delta^+_{y_{min}}/\Delta^+_{y_{max}}$	0.05/4.4	0.19/2.89	0.1/5.9	0.65/7.9	0.67/8.2	0.8/9.5

Table 1: Parameters of the simulations and reference test cases.

time average

$$< \varphi > (|y|) = \frac{1}{2t_{\rm av}L_xL_z} \int_{t_{\rm st}}^{t_{\rm st}+t_{\rm av}} \int_0^{L_x} \int_0^{L_z} (\varphi(t,x,-|y|,z) + \varphi(t,x,|y|,z))\, dz\, dx\, dt.$$

In Table 2, the mean flow quantities at the wall and at the channel centerline, denoted by the subscripts w and c, respectively, are compared with the reference DNS results.

The isotropic dynamic model has shown a very unstable behaviour at $Ma = 1.5$, so that no results are presented here for the isotropic dynamic model in this case. This kind of behaviour is usually handled in the literature by averaging the model coefficients in time and/or over homogeneity directions, as suggested in [21]. On the contrary, in this paper we have only employed averages over the local element, with the goal of assessing the performance of methods that should be applicable to complex turbulent flows, in which no homogeneity directions are easily identifiable. Although the isotropic dynamic model may possibly achieve stability after proper averaging of the coefficient, we see this behaviour as an indicator of the superior robustness of the anisotropic approach.

The wall stress relative errors range between $5 \div 25\%$, where the larger values are obtained with the Smagorinsky model. The Reynolds number Re_τ and the skin-friction velocity u_τ are affected by the wall shear stress error and by the fact that the density $\rho_{\rm w}$ at the wall is always underpredicted. On the other hand, at the center of the channel density values are higher than the reference ones and, coherently, temperature values are lower. The mean velocity at the centerline is always underestimated, except for the compressible cases computed with the Smagorinsky model. The overprediction of this quantity by the Smagorinsky model is probably related to its difficulties in connecting properly the wall region to the the logarithmic layer. At $Ma = 0.2$ and 0.7 the isotropic dynamic model represents a little better the wall stress and related quantities, but it performs worse with respect to density and temperature. In the simulations at $Ma = 0.2$, the constant density and temperature conditions of the incompressible MKM DNS are recovered with an error of the order of 4‰ at most. The wall shear stress $\tau_{\rm w}$ is the most sensitive quantity and is always underestimated. Looking at the mean quantities, for all the Mach numbers and all indicators considered, the dynamic models perform globally better than the Smagorinsky model in this VMS framework.

In Figure 1, the mean profiles corresponding to the mean density values reported in Table 2 are displayed. The excess in the density profiles at the channel center is related to the temperature values, which are lower than the DNS ones far from the wall, see Figure 2. The profiles of these quantities for the $Ma = 0.2$ are almost constant and have not been displayed. Figure 3 shows instead the mean velocity profiles, from which it is evident that the

	τ_w	Re_τ	u_τ/U_b	ρ_w/ρ_b	U_c/U_b	ρ_c/ρ_b	ρ_c/ρ_w	T_c/T_w
MKM	11.21	178	0.0635	—	1.17	—	—	—
Anis. dyn. Ma02	10.38	171	0.0608	1.001	1.15	0.999	0.999	1.005
Iso. dyn. Ma02	10.62	172	0.0614	1.001	1.15	0.999	0.998	1.005
Smag. Ma02	9.98	167	0.0596	1.004	1.16	0.999	0.996	1.005
WP	12.38	186	0.0618	1.107	1.16	0.995	0.925	1.086
Anis. dyn. Ma07	10.31	176	0.0588	1.068	1.15	0.996	0.933	1.070
Iso. dyn. Ma07	10.73	178	0.0608	1.060	1.15	0.998	0.942	1.061
Smag. Ma07	9.20	166	0.0555	1.067	1.17	0.996	0.9333	1.070
CKM	12.12	222	0.0545	1.358	1.164	0.982	0.723	1.378
Anis. dyn. Ma15	10.62	202	0.0527	1.280	1.161	0.990	0.776	1.284
Smag. Ma15	9.94	196	0.0505	1.299	1.174	0.985	0.758	1.313

Table 2: Mean flow quantities for all the numerical experiments.

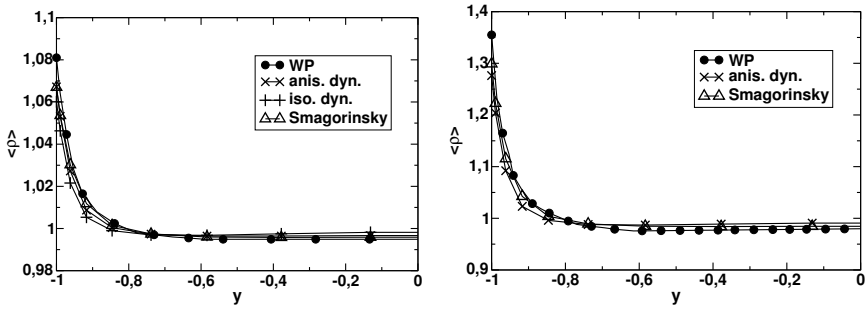

(a) (b)

Figure 1: Mean density profiles at (a) $Ma = 0.7$ and (b) $Ma = 1.5$.

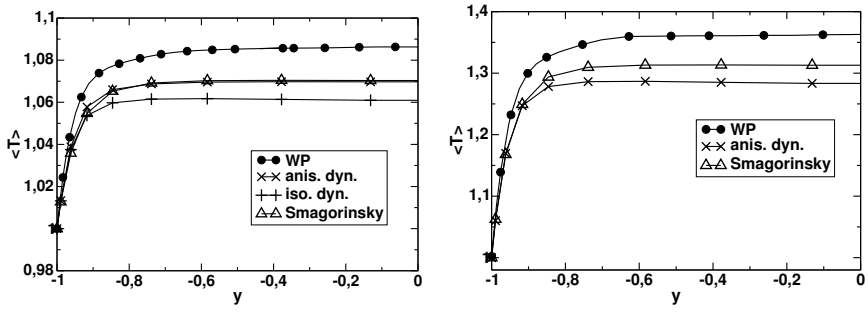

(a) (b)

Figure 2: Mean temperature profiles at (a) $Ma = 0.7$ and (b) $Ma = 1.5$.

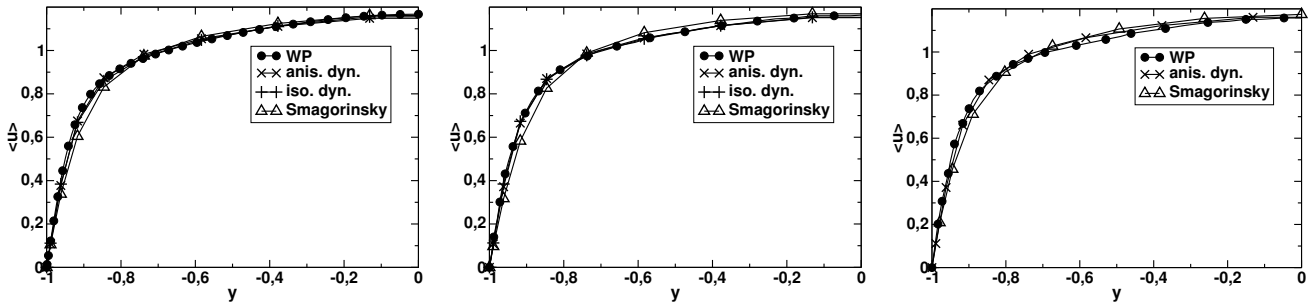

(a) (b) (c)

Figure 3: Mean streamwise velocity profiles at (a) $Ma = 0.2$, (b) $Ma = 0.7$ and (c) $Ma = 1.5$.

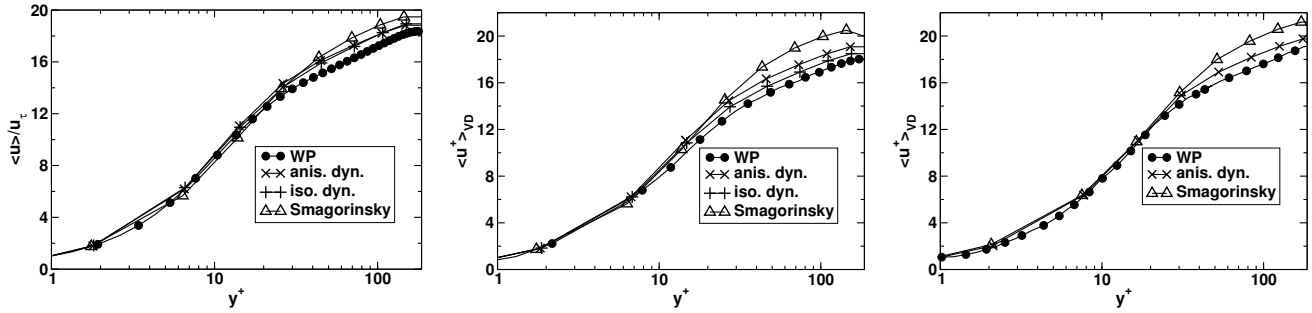

(a) (b) (c)

Figure 4: Mean streamwise velocity profiles in wall unit representation at (a) $Ma = 0.2$, (b) $Ma = 0.7$ and (c) $Ma = 1.5$.

dissipative nature of the Smagorinsky model causes an underestimation of the velocity in the buffer region and its the overprediction in the channel center. To enhance the difference between the subgrid scale models, in Figure 4 we report the mean velocity profile in wall unit representation and following the Van Driest transformation [25]

$$\langle u \rangle^+_{VD} = \int_0^{\langle u \rangle^+} \left(\frac{\langle \rho \rangle}{\rho_{\rm w}} \right)^{1/2} d\langle u \rangle^+ \tag{74}$$

for $Ma = 0.7$ and 1.5. The results for the two dynamic models are similar for $Ma = 0.2$, but at $Ma = 0.7$ the isotropic model shows a little better agreement with DNS than the anisotropic one, which in turn has good agreement at $Ma = 1.5$.

Figure 5 shows the mean profile of the non-solenoidal term $\partial_y < v >$ in the supersonic case. With the anisotropic model, the compression is very well reproduced near the wall, while this is not the case for the Smagorinsky model. In the buffer region, the dilatation is shifted forward for both models.

In Figures 6-8, the root mean square values of the resolved velocity fluctuations are displayed. In the incompressible limit, Figure 6 for the streamwise turbulence intensity shows that the dissipative nature of the Smagorinsky model always leads to an underprediction of the streamwise turbulence intensity near the wall, and too high fluctuations in the buffer and central region. We recall that these quantities represent the resolved contributions only, so that their overestimation with respect to the DNS value is an undesired result. On the other hand, the streamwise fluctuations are always well reproduced by the anisotropic model and, where it is available, by the isotropic dynamic one. The fluctuations of the velocity components normal to the wall (Figure 7) and spanwise (Figure 8) in the wall region are underestimated by both dynamic models with

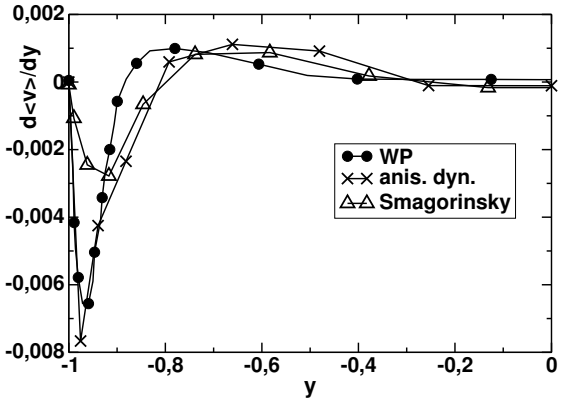

Figure 5: Mean dilatation profiles at $Ma = 1.5$.

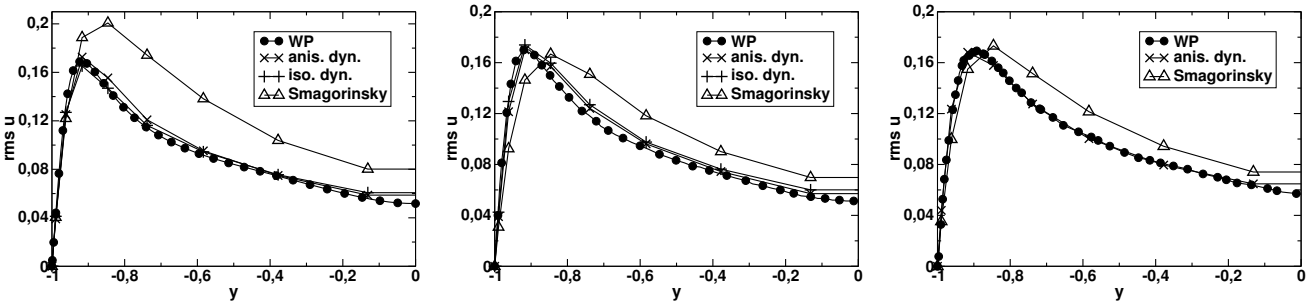

(a) (b) (c)

Figure 6: Root mean square profiles of the streamwise velocity component at (a) $Ma = 0.2$, (b) $Ma = 0.7$ and (c) $Ma = 1.5$.

respect to the DNS values, although we recall that these are the resolved contribution only.

In Figure 9 results for the total (modelled plus resolved) turbulent kinetic energy are displayed. For the Smagorinsky model, this corresponds to the resolved turbulent kinetic energy, since the isotropic part of the subgrid stresses is neglected. It can be observed that also for this quantity the DNS results are very well reproduced by the dynamic models.

Since during the simulations a constant mass flow is imposed, the wall shear stress τ_{w} can differ from the expected DNS value (see Table 2) and relevant differences also affect the wall normal turbulent shear stress (modeled + resolved) reported in Figure 10. Here, the stress is rescaled by the corresponding u_τ wall friction velocity obtained in each simulation and, in the cases $Ma = 0.7$ and $Ma = 1.5$, weighted by the local density. In spite of the application of the damping function, the Smagorinsky model does not present the correct trend at the wall and the shear stress is overestimated. This behaviour is probably the cause of the underprediction of the mean velocity profile in the wall region and of the difficulties in connecting properly the wall region to the the logarithmic layer. On the other hand, the dynamic models are in quite good agreement with the DNS results for simulations at all Mach numbers.

4.2. Channel flow over periodic hills

To evaluate the performance of the implemented subgrid scale models in a more complex setting, in which e.g. separation and reattachment arise and a less trivial geometry is considered, turbulent channel flow over a periodic hill has been simulated. First studied in [3], the periodic hill flow has become an important test case for CFD and

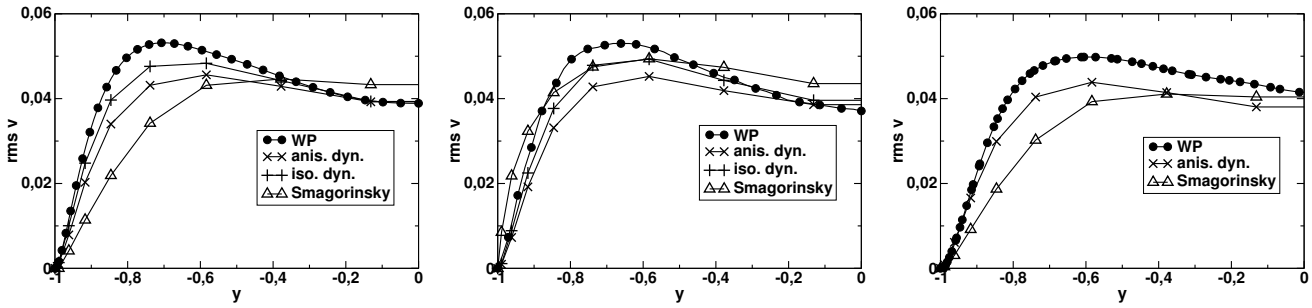

(a) (b) (c)

Figure 7: Root mean square profiles of the wall normal velocity component at (a) $Ma = 0.2$, (b) $Ma = 0.7$ and (c) $Ma = 1.5$.

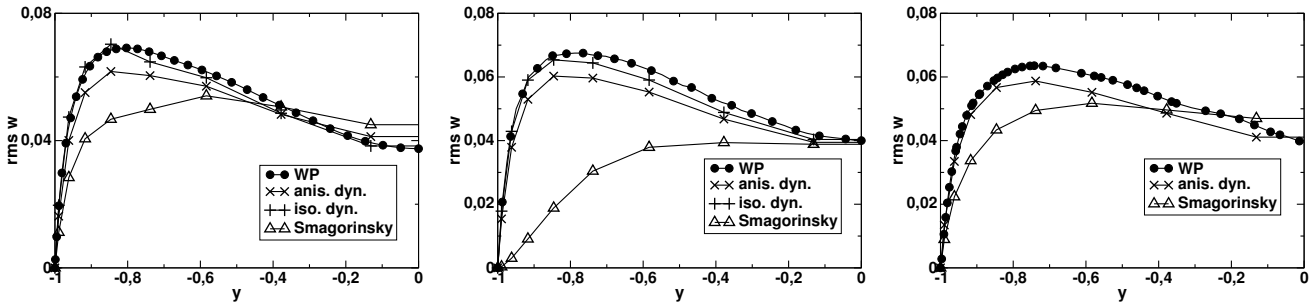

(a) (b) (c)

Figure 8: Root mean square profiles of the spanwise velocity components at (a) $Ma = 0.2$, (b) $Ma = 0.7$ and (c) $Ma = 1.5$.

in particular for RANS and LES simulations that has been discussed e.g. in a number of ERCOFTAC workshops. Despite the apparently simple geometry, the periodic hill test case presents some challenging feature, like the massive flow separation from a curved surface, the high sensitivity of the reattachment point location to the separation and the strong acceleration of the flow. Most of the results in the published literature refer to the incompressible case [6], [17], while we refer to the compressible simulation results reported in [61] and we employ the modified geometry defined in [41]. For this test, only the performance of the dynamic models has been assessed, considering the generally inferior performance of the simpler Smagorinsky model in the previous plane channel test case.

The computational domain (Fig. 11(a)) is a periodic plane channel constricted by a hill of height h about one third of the total channel height. Domain dimensions are: $L_x = 9.0h$ for streamwise direction , $L_z = 4.5h$ for spanwise direction and $L_y = 3.036h$ for the height. The mesh is composed of two regions, with a conforming matching. A structured hexahedral mesh, where each hexahedron is divided into 6 tetrahedra, is used to resolve the boundary layer close to the hill profile, while a fully unstructured, three-dimensional mesh is used in the bulk region. A two-dimensional section of the resulting mesh is shown in Figure 11(b). The total number of elements is 16662. For the structured, boundary layer mesh, we have $N_z = 12$ elements in the spanwise direction, which, using basis functions of degree $q = 4$, leads to a $\Delta z/h \simeq 0.062$. In order to accurately describe the hill shape, the streamwise resolution varies from $\Delta x/h \simeq 0.062$ between the two hills to $\Delta x/h \simeq 0.023$ at the top of the hill. The mesh is refined in the normal direction to reach $\Delta y/h \simeq 0.0032$ at the bottom wall, whereas no mesh refinement has been applied

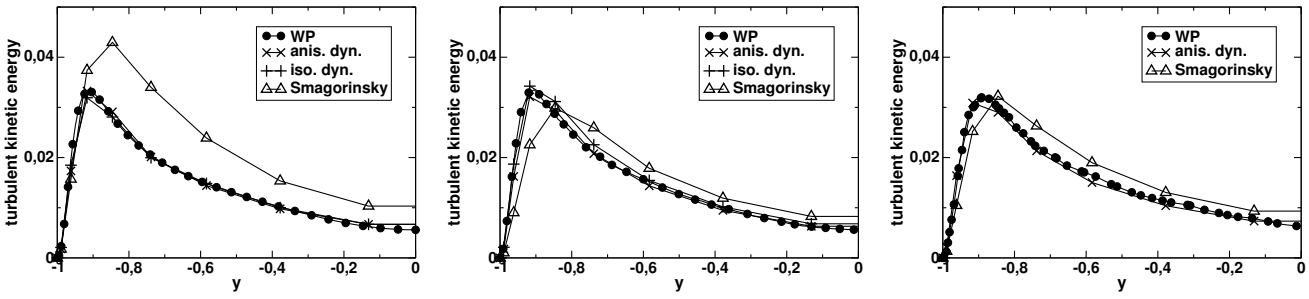

(a) (b) (c)

Figure 9: Total modelled+resolved turbulent kinetic energy at (a) $Ma = 0.2$, (b) $Ma = 0.7$ and (c) $Ma = 1.5$.

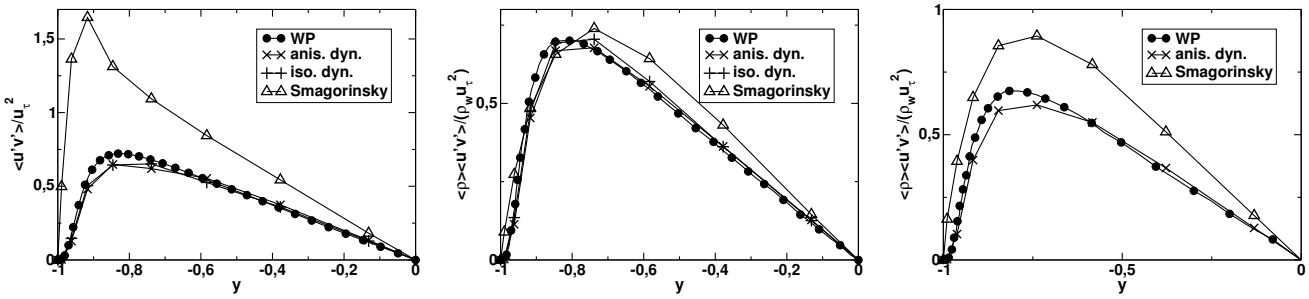

(a) (b) (c)

Figure 10: Total modelled+resolved turbulent wall normal shear stress at (a) $Ma = 0.2$, (b) $Ma = 0.7$ and (c) $Ma = 1.5$. The stress is normalized by the corresponding u_τ wall friction velocity obtained by the simulation.

close to the upper wall.

The no-slip and isothermal wall boundary conditions are imposed at both upper and lower surfaces. Cyclic boundary conditions are imposed in the streamwise and spanwise directions where the flow is assumed to be periodic. As in the channel flow simulation, a varying in time driving force is applied to keep constant mass flow. The bulk Reynolds and Mach numbers, defined as

$$Re_{\rm b} = \frac{\rho_{\rm b}^{\rm d} U_{\rm b}^{\rm d} d^{\rm d}}{\mu_{\rm w}^{\rm d}}, \qquad Ma_{\rm b} = \frac{U_{\rm b}^{\rm d}}{\sqrt{\gamma R T_{\rm w}^{\rm d}}}, \tag{75}$$

are imposed *a priori*, where $U_{\rm b}^{\rm d}$ and $\rho_{\rm b}^{\rm d}$ are respectively the bulk velocity and density evaluated on the crest of the hill, and $T_{\rm w}$ and $\mu_{\rm w}^{\rm d}$ are the temperature and the viscosity at the wall. The values we have employed are $Re_{\rm b} = 2800$ and $Ma_{\rm b} = 0.2$. The results are compared with those obtained by [6] in an incompressible direct numerical simulation.

A first view of the results is provided in Figure 4.2, in which the averaged values of the streamwise velocity componen are displayed along the channel, as computed using the anisotropic dynamic model. The size and the position of the flow separation region compare very well with the DNS results reported in the literature. Furthermore, for a more detailed assessment, we show profiles of velocities and turbulent stress averaged over the spanwise direction and time at four different positions in the flow field, also shown in Figure 11(b). The time average considered an interval of at least 50 non dimensional time units. The first profile at $x/h = 0.5$ is located just after the separation and through the strong shear layer; the second at $x/h = 2$, at the beginning of the flat floor, is inside the main recirculation bubble, while the third one at $x/h = 4$ is at its end. Finally, the fourth one at $x/h = 6$ is located in the reattached flow region. In Figure 13(a) the mean streamwise velocity profiles, for both the dynamic models, show an

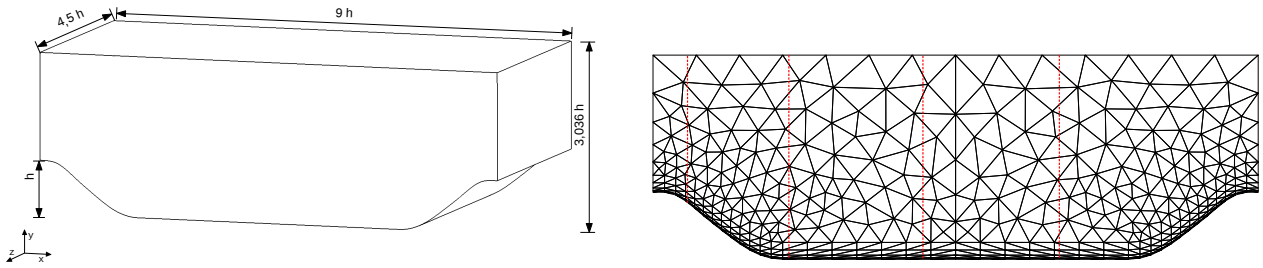

(a) (b)

Figure 11: (a) Periodic hill geometry with $L_x = 9.0h$, $L_z = 4.5h$,$L_y = 3.036h$ (b) section in the $(x-y)$ plane of the mesh used for the periodic hill simulations; the dotted lines at $x/h = 0.5, 2, 4, 6$ denote the positions of the mean profiles displayed in the following figures.

excellent agreement with DNS results. Some discrepancies are presented in the normal to the wall mean velocity profiles in Figure 14 where the dynamic isotropic model performs a little better than the anisotropic one in the main separation bubble. However, the normal velocity is very small and the errors are lower than two percent of the bulk velocity. The total, resolved plus modeled, turbulent stresses in Figure 15-17 are slightly better reproduced by the anisotropic model. The spanwise component $< u_i' u_j' >$ of normal stresses is overestimated by both the dynamic models in the flat region between the hills. The positions of the peaks in all the profiles and the shape of the shear layer are well captured by both dynamic models.

5. Conclusions and future perspectives

We have investigated the potential benefits resulting from the application of the anisotropic dynamic model [2] in the context of a high order DG model for compressible flow LES. This approach contrasts with other attempts at implementing LES in a DG framework, in which only Smagorinsky closures have been applied so far. Furthermore, the hierarchical nature of the DG finite element basis was exploited to implement the LES grid and test filters via projections on the finite dimensional subspaces that define the numerical approximation, along the lines of similar proposals in the VMS framework. A comparison with the DNS experiment results reported in [9], [43] and [58] for a plane channel and in [6] for a constricted channel has been carried out. In the plane channel case, the results of the comparison show a clear improvement in the prediction of several key features of the flow with respect to the Smagorinsky closure implemented in the same framework. The proposed approach appears to lead to significant improvements both in the low and high Mach number regimes. In particular, the anisotropic model appears to be more robust than the isotropic model for high Mach number regimes, where the isotropic model is unstable is simple elementwise averaging of the model coefficients is employed. The results of the constricted channel flow at low Mach number, on the other hand, displayed much less sensitivity to the choice of the subgrid model.

On this basis, we plan to investigate further extensions of this approach to flows in presence of gravity, with the goal of improving the turbulence models for applications to environmental stratified flows. Furthermore, the numerical framework that has been validated by the comparison reported in this paper will be employed for the assessment of the proposal presented in [42] for the extension of the eddy viscosity model to compressible flows.

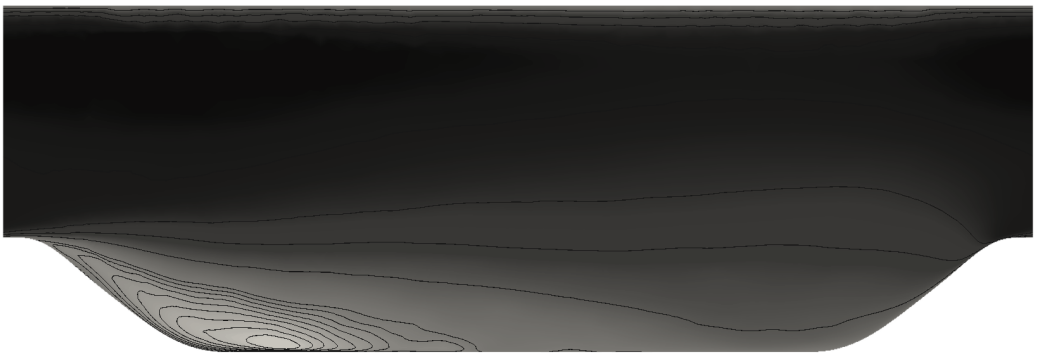

Figure 12: Averaged streamwise velocity in the period hill flow test case.

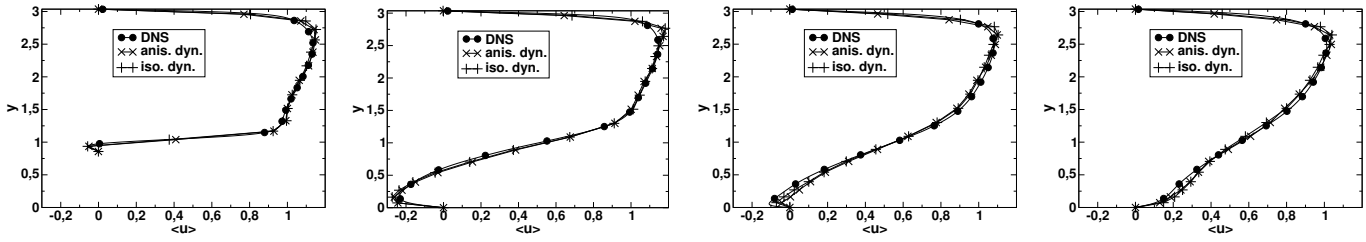

Figure 13: Mean streamwise velocity profiles in the periodic hill flow test case at different locations along the channel; (a): $x/h = 0.5$; (b): $x/h = 2$; (c): $x/h = 4$; (d): $x/h = 6$.

Acknowledgements

We would like to thank an anonymous referee for some useful remarks which helped to improve the initial version of this paper. Part of the results have been already presented in the Master thesis in Aerospace Engineering of A. Maggioni, prepared at Politecnico di Milano under the supervision of some of the authors. We would like to thank A. Maggioni for the first implementation of the dynamic models we have employed in this work. We are also very grateful to M.Germano for several useful discussions on the topics studied in this paper and several comments that helped to improve the presentation of our results. The present research has been carried out with financial support by Regione Lombardia and by the Italian Ministry of Research and Education in the framework of the PRIN 2008 project *Analisi e sviluppo di metodi numerici avanzati per Equazioni alle Derivate Parziali.* We acknowledge that the results of this research have been achieved using the computational resources made available at CINECA (Italy) by the high performance computing projects ISCRA-C HP10CAM1FM and HP10CVWE4N.

[1] A. Abbà, C. Cercignani, G. Picarella, and L. Valdettaro. A 3d turbulent boundary layer test for les models. In *Computational Fluid Dynamics 2000*, 2001.

[2] A. Abbà, C. Cercignani, and L. Valdettaro. Analysis of Subgrid Scale Models. *Computer and Mathematics with Applications*, 46:521–535, 2003.

[3] G.P. Almeida, D.F.G. Durao, and M.V. Heitor. Wake flows behind two-dimensional model hills. *Experimental Thermal and Fluid Science*, 3:87–101, 1999.

[4] D.N. Arnold, F. Brezzi, B. Cockburn, and L.D. Marini. Unified analysis of Discontinuous Galerkin methods for elliptic problems. *SIAM Journal of Numerical Analysis*, 39:1749–1779, 2002.

[5] F. Bassi and S. Rebay. A High Order Accurate Discontinuous Finite Element Method for the Numerical Solution of the Compressible Navier-Stokes Equations. *Journal of Computational Physics*, 131:267–279, 1997.

[6] M. Breuer, N. Peller, C. Rapp, and M. Manhart. Flow over periodic hills - numerical and experimental study in a wide range

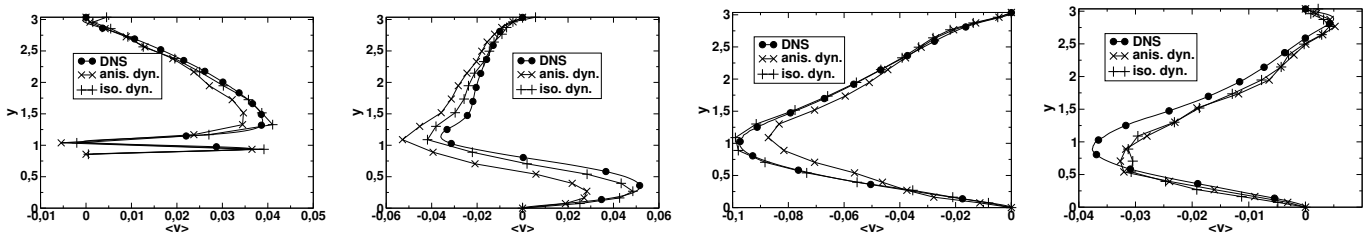

(a) (b) (c) (d)

Figure 14: Mean normal velocity profiles in the periodic hill flow test case at different locations along the channel;; (a): $x/h = 0.5$; (b): $x/h = 2$; (c): $x/h = 4$; (d): $x/h = 6$.

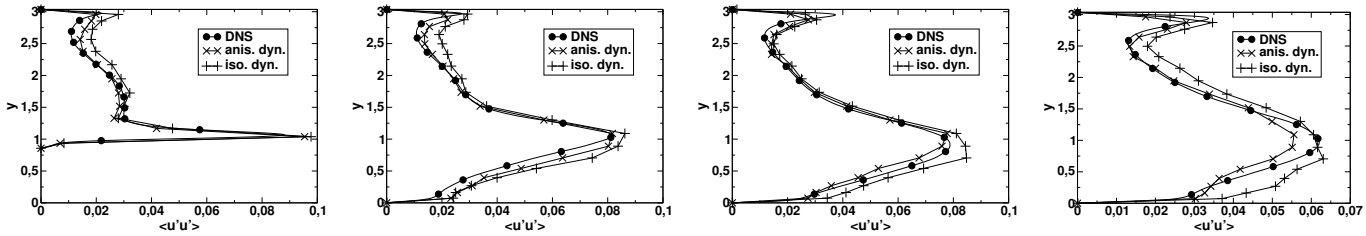

(a) (b) (c) (d)

Figure 15: Streamwise component of normal total (resolved + modeled) turbulent stresses profiles in the periodic hill flow test case at different locations along the channel; (a): $x/h = 0.5$; (b): $x/h = 2$; (c): $x/h = 4$; (d): $x/h = 6$.

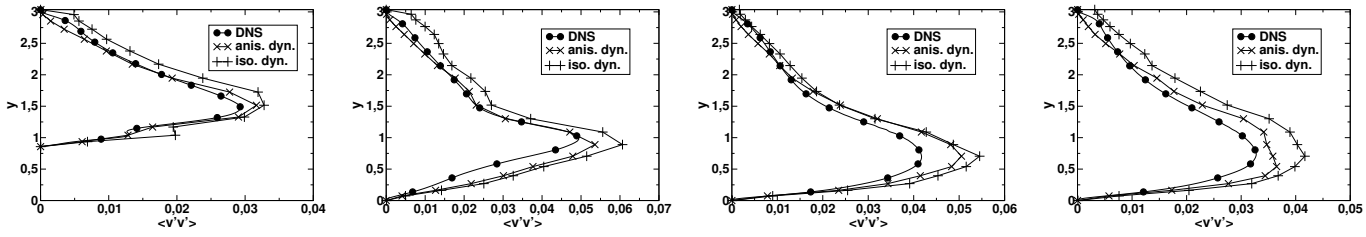

(a) (b) (c) (d)

Figure 16: Normal total (resolved + modeled) turbulent stresses profiles in the periodic hill flow test case at different locations along the channel; (a): $x/h = 0.5$; (b): $x/h = 2$; (c): $x/h = 4$; (d): $x/h = 6$.

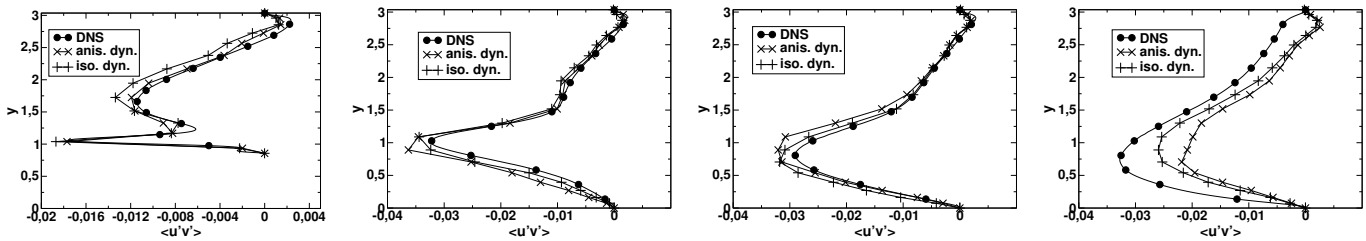

(a) (b) (c) (d)

Figure 17: Shear total (resolved + modeled) turbulent stresses profiles in the periodic hill flow test case at different locations along the channel; (a): $x/h = 0.5$; (b): $x/h = 2$; (c): $x/h = 4$; (d): $x/h = 6$.

of reynolds numbers. *Computers & Fluids*, 38:33–457, 2009.

[7] P. Castillo, B. Cockburn, I. Perugia, and D. Schötzau. An a priori analysis of the Local Discontinuous Galerkin method for elliptic problems. *SIAM Journal of Numerical Analysis*, 38:1676–1706, 2000.

[8] B. Cockburn and C. Shu. The Local Discontinuous Galerkin Method for Time-Dependent Convection-Diffusion Systems. *SIAM Journal of Numerical Analysis*, 35:2440–2463, 1998.

[9] G.N. Coleman, J. Kim, and R.D. Moser. A numerical study of turbulent supersonic isothermal-wall channel flow. *Journal of Fluid Mechanics*, 305:159–183, 1995.

[10] S. S. Collis. Discontinuous Galerkin methods for turbulence simulation. In *Proceedings of the 2002 Center for Turbulence Research Summer Program*, pages 155–167, 2002.

[11] S. S. Collis and Y. Chang. The DG/VMS method for unified turbulence simulation. *AIAA paper*, 3124:24–27, 2002.

[12] R. Cools. An Encyclopaedia of Cubature Formulas. *Journal of Complexity*, 19:445–453, 2003.

[13] F.van der Bos, J.J.W. van der Vegt, and B.J. Geurts. A multiscale formulation for compressible turbulent flows suitable for general variational discretization techniques. *Computer Methods in Applied Mechanics and Engineering*, 196:2863–2875, 2007.

[14] T.M. Eidson. Numerical simulation of turbulent rayleigh-bénard problem using subgrid modeling. *Journal of Fluid Mechanics*, 158:245–268, 1985.

[15] G. Erlebacher, M.Y. Hussaini, C.G. Speziale, and T.A. Zang. Large-eddy simulation of compressible turbulent flows. *Journal of Fluid Mechanics*, 238:155–185, 1992.

[16] FEMilaro, a finite element toolbox. `https://code.google.com/p/femilaro/`. Available under GNU GPL v3.

[17] J. Fröhlich, C.P. Mellen, W. Rodi, L.Temmerman, and M.A. Leschziner. Highly resolved large-eddy simulation of separated flow in a channel with streamwise periodic constrictions. *JFM*, 526:19–66, 2005.

[18] F. Garcia, L. Bonaventura, M. Net, and J. Sánchez. Exponential versus IMEX high-order time integrators for thermal convection in rotating spherical shells. *Journal of Computational Physics*, 264:41–54, 2014.

[19] E. Garnier, N. Adams, and P. Sagaut. *Large Eddy Simulation for Compressible Flows*. Springer Verlag, 2009.

[20] M. Germano. Turbulence: the filtering approach. *Journal of Fluid Mechanics*, 238:325–336, 1992.

[21] M. Germano, U. Piomelli, P. Moin, and W. H. Cabot. A Dynamic Subgrid-Scale Eddy Viscosity Model. *Physics of Fluids*, 3(7):1760–1765, 1991.

[22] G. Gibertini, A. Abbà, F. Auteri, and M. Belan. Flow around two in-tandem flat plates: Measurements and computations comparison. In *5th International Conference on Vortex Flows and Vortex Models (ICVFM2010)*, 2010.

[23] F.X. Giraldo and M. Restelli. A study of spectral element and discontinuous Galerkin methods for the Navier-Stokes equations in nonhydrostatic mesoscale atmospheric modeling: equation sets and test cases. *Journal of Computational Physics*, 227:3849–3877, 2008.

[24] F.X. Giraldo, M. Restelli, and M. Läuter. Semi-implicit formulations of the Navier-Stokes equations: application to nonhydrostatic atmospheric modeling. *SIAM Journal of Scientific Computing*, 32:3394–3425, 2010.

[25] P.G. Huang and G.N. Coleman. Van driest transformation and compressible wall-bounded turbulent flows. *AIAA J.*, 32:2110–2113, 1994.

[26] T.J.R. Hughes, G.R. Feijoo, L. Mazzei, and J.B. Quincy. The variational multiscale method-a paradigm for computational mechanics. *Computer Methods in Applied Mechanics and Engineering*, 166:3–24, 1998.

[27] T.J.R. Hughes, L. Mazzei, and K. Jansen. Large Eddy Simulation and the variational multiscale method. *Computing and Visualization in Science*, 3:47–59, 2000.

[28] T.J.R. Hughes, L. Mazzei, A.A. Oberai, and A.A. Wray. The multiscale formulation of large eddy simulation: Decay of homogeneous isotropic turbulence. *Physics of Fluids*, 13:505–512, 2001.

[29] T.J.R. Hughes, A.A. Oberai, and L. Mazzei. Large eddy simulation of turbulent channel flows by the variational multiscale method. *Physics of Fluids*, 13:1784–1799, 2001.

[30] T.J.R. Hughes, G. Scovazzi, and L.P. Franca. *Multiscale and stabilized methods*. Wiley, 2004.

[31] V. John and A. Kindl. Numerical studies of finite element Variational Multiscale Methods for turbulent flow simulations. *Computer Methods in Applied Mechanics and Engineering*, 199:841–852, 2010.

[32] V. John and M. Roland. Simulations of the turbulent channel flow at $Re_\tau = 180$ with projection-based finite element Variational Multiscale Methods. *International Journal of Numerical Methods in Fluids*, 55:407–429, 2007.

[33] D. Knight, G. Zhou, N. Okong'o, and V.Shukla. Compressible large eddy simulation using unstructured grids. Technical Report 98-0535, American Institute of Aeronautics and Astronautics, 1998.

[34] B. Koobus and C. Farhat. A variational multiscale method for the large eddy simulation of compressible turbulent flows on unstructured meshes—-application to vortex shedding. *Computer Methods in Applied Mechanics and Engineering*, 193:1367–1383, 2004.

[35] J. Lander and B.J. Hoskins. Believable scales and parameterizations in a spectral transform model. *Monthly Weather Review*, 125:292–303, 1997.

[36] B. Landmann, M. Kessler, S. Wagner, and E. Krämer. A parallel, high-order discontinuous galerkin code for laminar and turbulent flows. *Computers & Fluids*, 37:427–438, 2008.

[37] E. Lenormand, P.Sagaut, and L. Ta Phuoc. Large eddy simulation of subsonic and supersonic channel flow at moderate reynolds number. *International Journal of Numerical Methods in Fluids*, 32:369–406, 2000.

[38] D. Lilly. A Proposed Modification of the Germano Subgrid-Scale Closure Method. *Physics of Fluids*, 4(3):633–635, 1992.

[39] A. Maggioni. Formulazione DG-LES per flussi turbolenti comprimibili: modelli e validazione in un canale piano. Master's thesis, School of Industrial Engineering, Politecnico di Milano, 2012.

[40] M. Pino Martin, U. Piomelli, and G.V. Candler. Subgrid-Scale Models for Compressible Large-Eddy Simulations. *Theoretical and Computational Fluid Dynamics*, 13:361–376, 2000.

[41] C. P. Mellen, J. Fröhlich, and W. Rodi. Large eddy simulation of the flow over periodic hills. In *16th IMACS World Congress*, Lausanne 2000.

[42] M.Germano, A. Abbà, R. Arina, and L. Bonaventura. On the extension of the eddy viscosity model to compressible flows. *Physics of Fluids*, 26(4):041702, 2014.

[43] R.D. Moser, J. Kim, and N.N. Mansour. Direct numerical simulation of turbulent channel flow up to $re_\tau = 590$. *Physics of Fluids*, 11:943–945, 1999.

[44] E.A. Munts, S.J. Hulshoff, and R. de Borst. A modal-based multiscale method for large eddy simulation. *Journal of Computational Physics*, 224:389–402, 2007.

[45] M. Restelli and F.X. Giraldo. A conservative Discontinuous Galerkin semi-implicit formulation for the Navier-Stokes equations in nonhydrostatic mesoscale modeling. *SIAM Journal of Scientific Computing*, 31:2231–2257, 2009.

[46] P. Sagaut. *Large Eddy Simulation for Incompressible Flows: An Introduction.* Springer Verlag, 2006.

[47] H. Schlichting. *Boundary-layer theory.7th edition.* McGraw-Hill, 1979.

[48] F.G. Schmitt. About Boussinesq's turbulent viscosity hypothesis: historical remarks and a direct evaluation of its validity. *Comptes Rendus Mécanique*, 335:617–627, 2007.

[49] J. C. Schulze, P. J. Schmid, and J. L. Sesterhenn. Exponential time integration using Krylov subspaces. *International Journal of Numerical Methods in Fluids*, 60:591–609, 2009.

[50] A. Scotti, C. Meneveau, and D. Lilly. Generalized Smagorinsky Model for Anisotropic Grids. *Physics of Fluids*, 5(9):2306–2308, 1993.

[51] K. Sengupta, F. Mashayek, and G.B. Jacobs. Large eddy simulation using a discontinuos galerkin spectral method. In *45th AIAA Aerospace Sciences Meeting and Exhibit.* AIAA, AIAA-2007-402 2007.

[52] R.J. Spiteri and S.J. Ruuth. A New Class of Optimal High-Order Strong-Stability-Preserving Time Discretization Methods. *SIAM Journal of Numerical Analysis*, 40:469–491, 2002.

[53] G. Tumolo and L. Bonaventura. A semi-implicit, semi-Lagrangian, DG framework for adaptive numerical weather prediction. *Quarterly Journal of the Royal Meteorological Society*, DOI:10.1002/qj.2544, 2015.

[54] G. Tumolo, L. Bonaventura, and M. Restelli. A semi-implicit, semi-Lagrangian, $p-$adaptive Discontinuous Galerkin method for the shallow water equations. *Journal of Computational Physics*, 232:4667, 2013.

[55] A. Uranga, P.O. Persson, M. Drela, and J. Peraire. Implicit Large Eddy Simulation of transition to turbulence at low Reynolds numbers using a Discontinuous Galerkin method. *International Journal for Numerical Methods in Engineering*, 87:232–261, 2011.

[56] F. van der Bos and B.J. Geurts. Computational error-analysis of a Discontinuous Galerkin discretization applied to large-eddy simulation of homogeneous turbulence. *Computer Methods in Applied Mechanics and Engineering*, 199:903–915, 2010.

[57] B. Vreman, B.J. Geurts, and H. Kuerten. .subgrid-modeling in LES of compressible flow. *Applied Scientific Research*, 54:191–203, 1995.

[58] L. Wei and A. Pollard. Direct numerical simulation of compressible turbulent channel flows using the Discontinuous Galerkin

method. *Computers and Fluids*, 47:85–100, 2011.

[59] K.S. Yang and J.H. Ferziger. Large-eddy simulation of turbulent obstacle flow using a dynamic subgrid-scale model. *AIAA Journal*, 31:1406–1413, 1993.

[60] A. Yoshizawa. Statistical theory for compressible turbulent flows with the application to subgrid modeling. *Physics of Fluids*, 29:2152–2164, 1986.

[61] D. You, S. T. Bose, and P. Moin. Grid-independent large-eddy simulation of compressible turbulent flows using explicit filtering. In *Center for Turbulence Research, Proceedings of the Summer Program*, 2010.

[62] Y. Zang, R.L. Street, and J.R. Koseff. A dynamic mixed subgrid-scale model and its application to turbulent recirculating flows. *Physics of Fluids*, 5:3186–3196, 1993.